


RESEARCH

Open Access



Model development and prediction of anti-icing longevity of asphalt pavement with salt-storage additive

Yan Zhang, Yong Deng and Xianming Shi* 

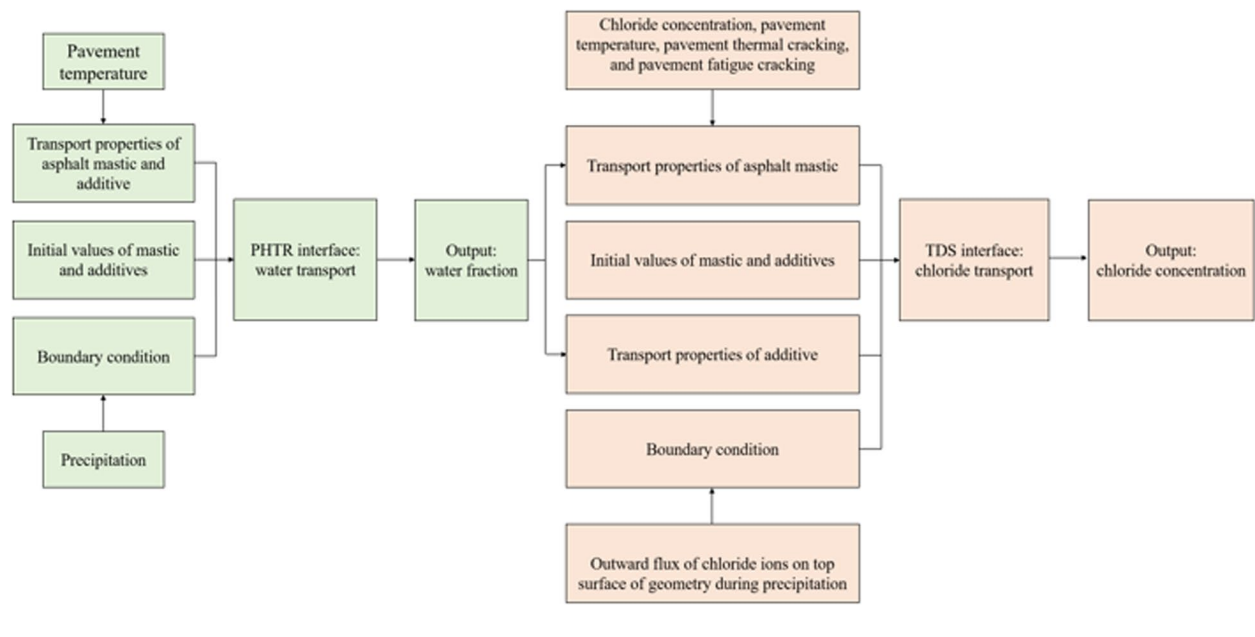
Abstract

This study established a systematic simulation framework to predict the anti-icing longevity of a thin overlay of asphalt pavement with salt-storage additive (APSSA). The water and chloride transport in the overlay when subjected to varying precipitation, temperature, thermal cracking, and fatigue cracking over time were modeled using a Finite Element Method based software. The simulation included two parts: water transport followed by chloride transport. Water transport that obeys the law of conservation of mass was modeled using the phase transport in porous media (phtr) interface of COMSOL, while chloride transport based on Fick's second law was modeled with the transport of diluted species (tds) interface. The simulation results show that the anti-icing function of a 16-mm thick overlay was fully effective in 2 years and 5 years for the minimum pavement temperature above -3.4°C and -2.4°C , respectively. These two pavement temperatures are equivalent to 97.4-percentile and 96.3-percentile of historical hourly pavement temperature near Pullman, Washington.

Keywords: Anti-icing, Service life, Asphalt overlay, Encapsulated salt, Finite element method, Water transport, Chloride transport, Model

*Correspondence: xianming.shi@wsu.edu
National Center for Transportation Infrastructure & Life-Extension,
Department of Civil & Environmental Engineering, Washington State
University, P. O. Box 642910, Pullman, WA 99164-2910, USA

Graphical abstract



Introduction

A few studies have reported that the anti-icing life of asphalt pavement with salt-storage additive (APSSA) can be calculated with predictive equations incorporating laboratory experiments [11, 24, 25, 55–58]. However, these estimations were overly simplified, rough, and inaccurate because of lack of a mechanistic model. Another significant deficiency of those predictions is neglect of a comprehensive consideration of the factors influencing the anti-icing life of APSSA, such as environmental conditions (e.g., precipitation and temperature) and pavement conditions (e.g., thermal cracking and fatigue cracking). Although many studies have worked on modeling ions (e.g., chloride) transport from the outside to the inside of cement concrete [2, 9, 18, 22, 31, 36, 49], no one has simulated outward ions (e.g., chloride) transport in asphalt pavement or cement concrete. No model has been developed to predict the anti-icing life of APSSA. Therefore, it is necessary to establish a systematic model for a more mechanistic and reliable prediction of the anti-icing life of APSSA.

The COMSOL Multiphysics is a cross-platform finite element method (FEM) based multiphysics simulation software. This software supports the simulation of designs involving single or coupled physics such as electromagnetics, structural mechanics, acoustics, fluid flow, heat transfer, chemical engineering, etc. [7, 17, 20, 26, 32, 36, 47]. Among them, the phase transport in porous media (phtr) interface in the subsurface flow module and the transport of diluted species (tds) interface in the

chemical reaction engineering module have been widely applied for simulating multi-phase flow (e.g., water–air flow) in porous media [28, 46, 48, 51] and simulating ionic ingress into cement concrete due to concentration gradient [2, 9, 22, 36, 49], respectively. For APSSA, ionic transport from the inside to the surface must be facilitated by water, and the process include two activities: water transport in asphalt mastic and salt-storage additive (SSA) followed by ion (e.g., chloride) transport due to concentration gradient. The two activities can be well modeled and linked by the cooperation of the two interfaces of the FEM software.

This work pioneered a numerical model with the COMSOL Multiphysics to predict the anti-icing life of a thin overlay of APSSA when subjected to varying precipitation, temperature, thermal cracking, and fatigue cracking over time. In this study, the APSSA sample used for the experiments to obtain the parameters of the model was asphalt mixture with 5.1 wt% laboratory-prepared functional additive (CaCl₂-zeolite/p-epoxy) #16. The additive was fabricated through a surface treatment approach, in which zeolite particles containing calcium chloride were coated by a microporous epoxy layer. The #16 denotes the gradation of the additive, which passed the sieve #16 and stayed on the sieve #30 (1.2 mm – 2.4 mm). More details of the preparation of CaCl₂-zeolite/p-epoxy #16 and the APSSA sample can be found in the laboratory study [53]. The simulation was separated into two steps, which are water transport into the overlay first then followed by chloride transport from the inside to the surface. The

water transport process follows the law of conservation of mass, while the chloride transport from high-concentration areas to low-concentration areas obeys Fick's second law.

Model description

To activate the anti-icing function of the functional additives in the overlay, there are two critical processes: 1) wetting of solid calcium chloride (CaCl_2) in the additives and 2) outward transport of the chloride ions. The wetting process is the one by which water intrudes into the asphalt mastic from the surface and finally enters the functional additives first through various pathways (e.g., pores and defects) in the overlay and then through the micropores on the epoxy coating layer. Subsequently, CaCl_2 turns from its combined state (i.e., solid CaCl_2 inside the additives) to ionic state (Ca cations and Cl anions dissolved in water) in the additives. Thereafter, the chloride ions in water migrate to the surface of the overlay through the same pathways of water ingress, mainly by diffusion (due to the chloride concentration gradient inside the overlay). The schematic illustration of the two processes is shown in Fig. 1.

In reality, the overlay counters wet-dry cycles due to weather variations over time. The wet-dry cycles lead to water–air transport in the overlay, which is a problem

of a two-phase flow in porous media that obeys the law of conservation of mass. On the other hand, Fick's second law is used to describe the transporting process of the chloride ions in the overlay, which is a non-steady state diffusion due to the chloride concentration gradient between the inside and the surface of the overlay.

Wet-dry cycles of the overlay

Sufficient water in the overlay is an essential precondition that makes the chloride ions being transported outward from inside of the additives to the surface of the overlay. The sources of water are rainfall in summer and snowfall in winter. To solve water–air phase transport in the overlay, the macroscopic mass conservation equation was used [3, 43, 44, 46]:

$$\frac{\partial}{\partial t} (\varepsilon_p \rho_i s_i) + \nabla \cdot (\rho_i \mathbf{u}_i) = 0 \quad (1)$$

where ε_p is the porosity of porous media, ρ_i is the density of phase i , s_i is the volume fraction of phase i , and \mathbf{u}_i is the volumetric flux (velocity vector) of phase i .

\mathbf{u}_i is determined with the extended Darcy's law as shown in Eq. 2 [5, 44]:

$$\mathbf{u}_i = -\frac{k_{ri}}{\mu_i} k (\nabla p_i - \rho_i \mathbf{g}) \quad (2)$$

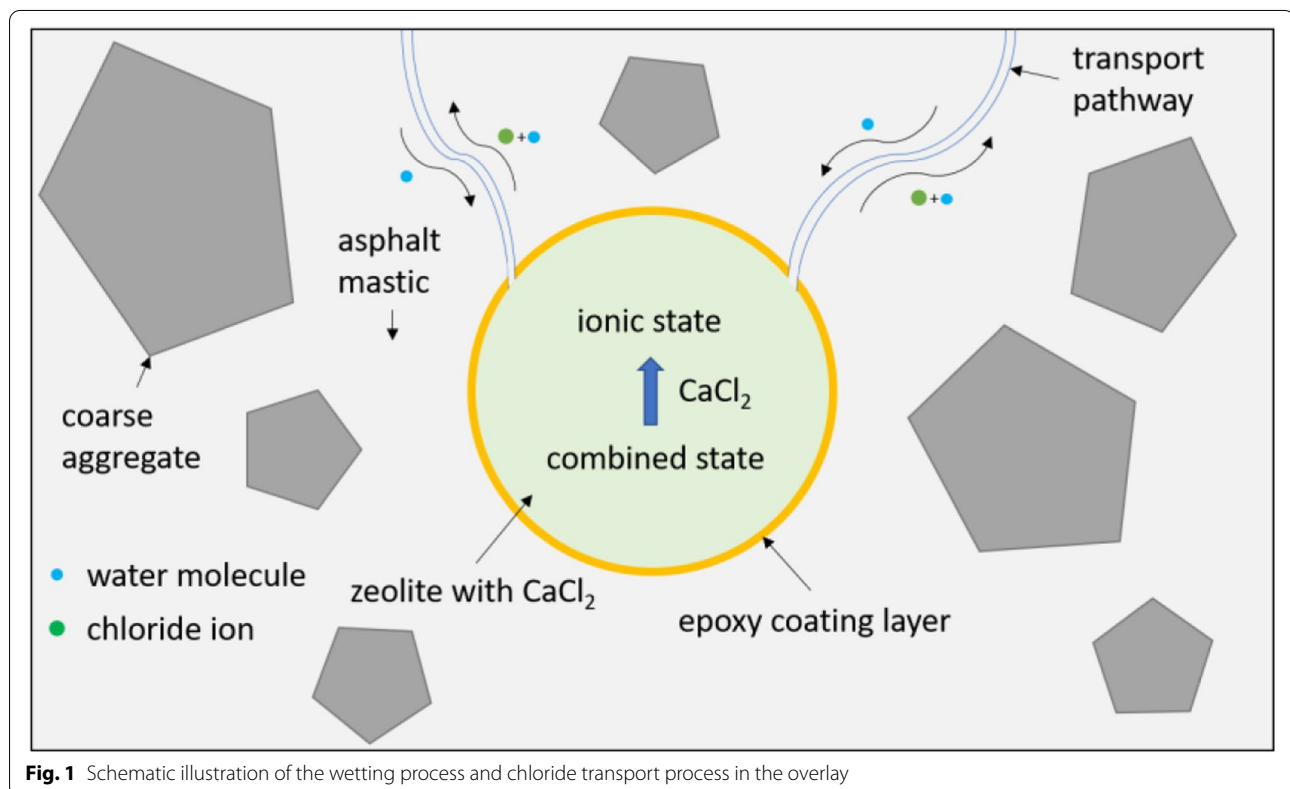


Fig. 1 Schematic illustration of the wetting process and chloride transport process in the overlay

where k_{ri} is the relative permeability of phase i , u_i is the dynamic viscosity of phase i , k is the permeability of porous media, p_i is the pressure field of phase i , and g is the gravitational acceleration vector.

The pressure difference across the interface between the non-wetting phase (e.g., air) and the wetting phase (e.g., water) is called capillary pressure (p_c), and the pressure of the non-wetting phase is greater than the pressure of the wetting phase because of the curvature and interfacial tension of the interface (Brooks and Corey, 1964; [43, 44, 46]:

$$p_c = (p_{s_n} - p_{s_w}) > 0 \quad (3)$$

where p_{s_n} is the pressure in the non-wetting phase, and p_{s_w} is the pressure in the wetting phase.

In the Brooks and Corey model, p_c depends on phase saturation as shown in Eq. 4 (Brooks and Corey, 1964, 1966; [46]:

$$p_c = p_{ec} \bar{s}_w^{-\frac{1}{\lambda_p}} \quad (4)$$

where \bar{s}_w is the effective volume fraction of the wetting phase, which is expressed as:

$$\bar{s}_w = \frac{s_w - s_{rw}}{1 - s_{rn} - s_{rw}} \quad (5)$$

where s_w is the volume fraction of the wetting phase, s_{rw} is the residual volume fraction of the wetting phase, and s_{rn} is the residual volume fraction of the non-wetting phase.

In the Brooks and Corey model, the relative permeability of the wetting phase (k_{rs_w}) and the non-wetting phase (k_{rs_n}) is expressed as Eqs. 6 and 7 (Brooks and Corey, 1964, 1966), respectively:

$$k_{rs_w} = \bar{s}_w^{(3+\frac{2}{\lambda_p})} \quad (6)$$

$$k_{rs_n} = \bar{s}_n^2 (1 - (1 - \bar{s}_n)^{(1+\frac{2}{\lambda_p})}) \quad (7)$$

where \bar{s}_n is the effective volume fraction of the non-wetting phase, which is expressed as:

$$\bar{s}_n = \frac{s_n - s_{rn}}{1 - s_{rn} - s_{rw}} \quad (8)$$

where s_n is the volume fraction of the non-wetting phase.

In the “phtr” interface, there are two phases in the model: the water phase and the air phase. The “phtr” interface solves for the averaged volume fraction of water and air. The dependent variables are the volume fraction of water (s_1) and the volume fraction of air (s_2).

The sum of the two volume fractions follows the volume constraint equation:

$$s_1 + s_2 = 1 \quad (9)$$

Equations 1 through 9 were implemented into the “phtr” interface of the COMSOL Multiphysics to simulate the water–air phase transport in overlay when exposed to weather variations.

Chloride transport

The transport of the chloride ions from high-concentration areas to low-concentration ones in the overlay obeys Fick’s second law, which is expressed as Eq. 10 [9, 19, 23]:

$$\frac{\partial C}{\partial t} = D \frac{\partial^2 C}{\partial x^2} \quad (10)$$

where C is chloride concentration, t is time, D is chloride diffusion coefficient, and x is a position variable.

In the “tds” interface of the COMSOL Multiphysics, Eq. 10 is written as Eqs. 11 and 12:

$$\frac{\partial C_i}{\partial t} + \nabla J_i = R_i \quad (11)$$

$$J_i = -D_i \nabla C_i \quad (12)$$

where C_i is the concentration of species i , t is time, J_i is diffusive flux vector, R_i is a reaction rate expression for species i ($R_i=0$ in this study), and D_i is the diffusion coefficient of species i .

Model assumptions

To simplify the modeling process, the following assumptions were proposed for the two-dimensional axisymmetric model in this study:

1. Asphalt mastic, and the additives are homogeneous, isotropic, and incompressible material.
2. The overlay simulated in the model has been constructed and started to be used on May 1, 2012.
3. The subbase layer under the overlay is an impermeable asphalt layer. Thus, no water or chloride ions flows into the subbase layer.
4. The effect of gravity is neglected for water transport.
5. CaCl_2 is not deposited on the surface and pores of the overlay.

Model settings in COMSOL multiphysics

Model geometry

Figure 2 depicts the geometries of the overlay in the model. Figure 2a is the cross-sectional image of an asphalt mixture specimen with 5.1 wt% CaCl_2 -zeolite/p-epoxy

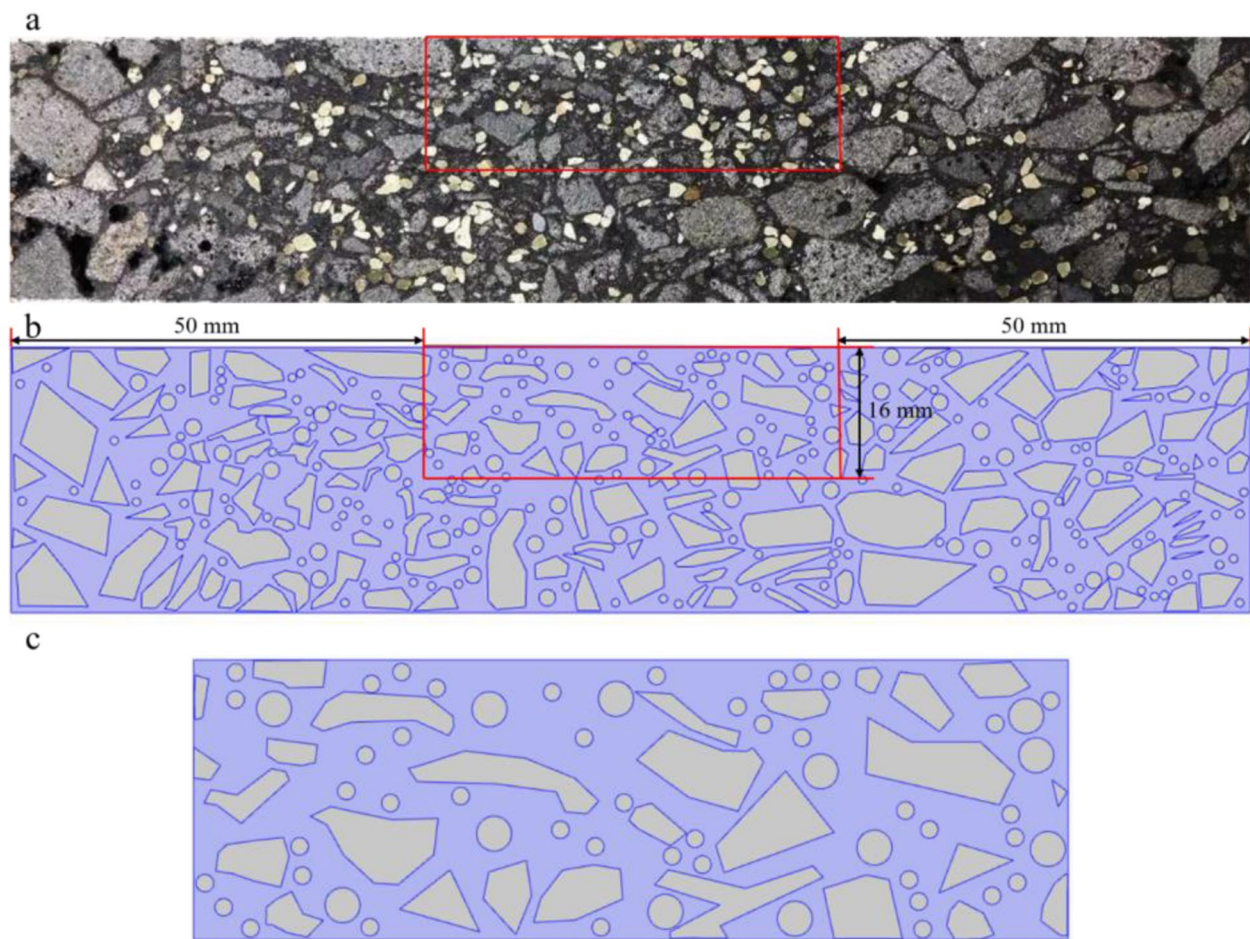


Fig. 2 **a** Original cross-sectional image of the asphalt mixture sample, **b** geometry used to determine thermal cracking-related coefficient and fatigue cracking-related coefficient to D of asphalt mastic, and **c** selected geometry for the simulations of water transport and chloride transport. (In Fig. 2b and c, gray circles are the CaCl_2 -zeolite/p-epoxy additives, gray irregular polygons are coarse aggregates, and purple area is asphalt mastic.)

#16. The dimension of the cross-section is $150 \text{ mm} \times 32 \text{ mm}$. The geometry of the model was pictured proportionally according to the original cross-sectional image with the aid of the computer-aided design and drafting software AutoCAD, as shown in Fig. 2b. The geometry in Fig. 2b was used to determine the thermal cracking-related coefficient and fatigue cracking-related coefficient of the chloride diffusivity of asphalt mastic. To simplify the geometry, the area in the red box in Fig. 2a and b was adopted for the simulations of water transport and chloride transport, as shown in Fig. 2c. In the Fig. 2b and c, the gray circles are CaCl_2 -zeolite/p-epoxy particles, the gray irregular polygons are coarse aggregates, and the purple area is the asphalt mastic. Two diameters of the additives were used: 1 mm for the small additives and 2 mm for the big additives. Three asphalt mixture samples were pictured, and the one with the median and thus representative levels of areas of mastic, aggregates,

and additives was selected for the modeling study. The software ImageJ was used to measure the areas of mastic, aggregates, and additives in each of the samples, and Table S1 shows the estimated values.

The coarse aggregates in the overlay were assumed to be highly impermeable and thus had little influence on the simulation results of water transport and chloride transport. Therefore, the domain of the coarse aggregates in the geometry was excluded from the simulations.

Phase transport in porous media (phtr) interface

Phase and porous media transport properties of asphalt mastic and additives

In the Brooks and Corey capillary pressure model, the entry capillary pressure (P_{ec}) can be estimated using Eq. 13 [16, 51]:

$$P_{ec} = \frac{2\sigma \cos\theta}{r_c} \quad (13)$$

where σ is interfacial tension of a fluid, θ is contact angle between the fluid and the capillary tube, and r_c is radius of the capillary tube. The σ of water is related to pavement temperatures with a unit of Kelvin (K) [10]. The temperature range for the data in the literature is from 5 °C to 45 °C. The plot of the relationship between the σ of water and pavement temperatures is shown in Figure S1. The contact angles of water to the epoxy layer and the asphalt mastic were measured using water contact angle test. For the pores in the epoxy layer on the surface of the additive, r_c is the average value of the pore's radii measured from scanning electron microscope (SEM) images. For the pores in asphalt mastic, the average r_c was calculated with Eq. 14 [41]:

$$r_c = \frac{2}{3} * \frac{AV\%}{100} * D_{75} \quad (14)$$

where AV% is air void percentage or porosity in asphalt mastic, and D_{75} is the particle-size diameter corresponding to 75% on the cumulative particle-size distribution curve of aggregates (Figure. S2). In the literature, the equation was determined based on the channel theory [38], which is suitable for asphalt pavement with an air void content of higher than 4%. According to Eq. 3, the positive value of the calculated P_{ec} of water in the pores of asphalt mastic was used in the model.

In the Brooks and Corey capillary pressure model, the pore size distribution index of the epoxy layer ($\lambda_{p-epoxy}$) on the surface of the additive was calculated using Eq. 15:

$$\lambda_{p-epoxy} = \frac{\Sigma(W_i * A_i)}{\Sigma(N_i * A_i)} \quad (15)$$

where W_i is the weight fraction of pores and $W_i = N_i * A_i / \Sigma(N_i * A_i)$, N_i is the number of pores, and A_i is the surface area of pores. N_i and A_i were obtained from SEM images (e.g., Fig. 3) of the surface of the additive with assisting with AutoCAD. An example of calculating the $\lambda_{p-epoxy}$ for Fig. 3 is shown in Table S2. Three SEM images were analyzed, and the results are shown in Table S3.

The pore size distribution index of asphalt mastic ($\lambda_{p-mastic}$) was calculated using Eq. 16 [33]:

$$\lambda_{p-mastic} = (333.3 * k_{mastic})^{0.154} \quad (16)$$

where k_{mastic} is the water permeability of asphalt mastic. Equation 16 was converted from Eq. 2, and the parameters in the equation were determined based on the results of the experiments conducted by the authors of the literature [33].

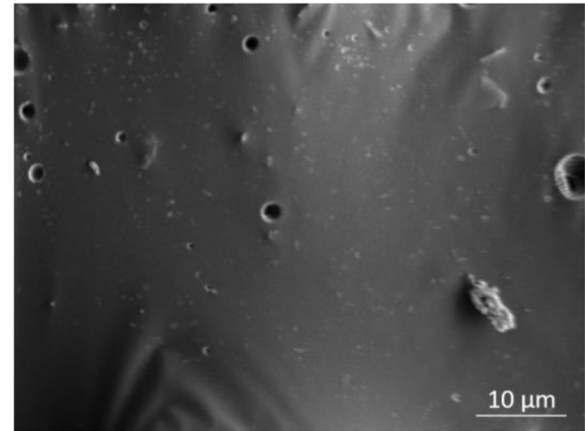


Fig. 3 Representative SEM image for measuring N_i and A_i on the surface of CaCl_2 -zeolite/p-epoxy #16

For simplicity, the density (ρ) of water was approximated to be 1000 kg/m³ for all pavement temperatures. The dynamic viscosity (μ) of water and the ρ and μ of air entailed three equations related to pavement temperatures with a unit of K [27, 42]. In the literature, the temperature range for the μ of water is from 0 °C to 60 °C at atmospheric pressure, and the equations for the ρ and μ of air are valid for a temperature range from -20 °C to 40 °C and a pressure of 1000 bm. The plots of the relationship between the properties and pavement temperatures are shown in Figures S3, S4 and S5. The determination of pavement temperature will be described in the Sect. 3.3.1. The residual saturation (s_r) of a water–air system was assumed to be 0 in this study.

The (average) porosity of the epoxy layer on the additive was 2.1%, which can be found in our previous study [53]. The water permeability of the epoxy layer was assumed to be a very small positive value, which was expressed as 'eps [m²]' in COMSOL Multiphysics.

The values or equations of the terms mentioned above are shown in Table 1.

Initial value and boundary condition

The initial value of the water volume fractions ($s_{0,sl}$) in the model was assumed to be 0.

The wet-dry cycles of the overlay are mainly affected by precipitations, which are the source of water driving chloride transport. Thus, the hourly data of precipitations including rainfalls and snowfalls from May 1, 2012 to November 27, 2020 was introduced into the model. The weather data at Pullman, Whitman County, Washington was obtained from "AgWeatherNet" of Washington State University (<https://weather.wsu.edu/>). In the model, the boundary condition on the top surface of the

Table 1 Values of items used to calculate or used as physical parameters in the model

Parameter	Value/Equation	Unit
σ of water	$2.67 \times T^{-0.633}$	N/m
θ of water on asphalt mastic	109	°
θ of water on the epoxy layer	77.5	°
Average r_c of additives	$2.50E-06$	m
AV% or porosity of asphalt mastic	7	%
Porosity of epoxy layer on additives	2.1	%
D_{75}	$8.70E-03$	m
$\lambda_{p-epoxy}$	0.220	NA
$\lambda_{p-mastic}$	1.54	NA
ρ of water	1000	kg/m ³
μ of water	$4E+13 \times T^{-6.72}$	Pa·s
s_r of water	0	NA
ρ of air	$348.48 \times T^{-1}$	kg/m ³
μ of air	$8E-06 \times e^{0.0028 \times T}$	Pa·s
s_r of air	0	NA
K_{mastic}	$5.19E-14$	m ²
Water permeability of epoxy layer on additives	eps	m ²

T Temperature in K, *eps* a very small positive value (10^{-15}), NA Not Applicable

geometry was that either the water volume fraction was 1 for precipitation or the water volume fraction was 0 for no precipitation, which can be implemented using an “Interpolation” function of COMSOL Multiphysics.

Transport of diluted species (tds) interface

Transport properties of asphalt mastic

For a one-dimensional finite diffusion problem, assuming the chloride concentration at surface is constant, the

analytical solution of the partial differential Eq. 10 can be expressed as Eq. 17 [9, 19, 22, 23]:

$$\frac{C(x, t) - C_0}{C_s - C_0} = 1 - \operatorname{erf}\left[\frac{x}{2\sqrt{Dt}}\right] \quad (17)$$

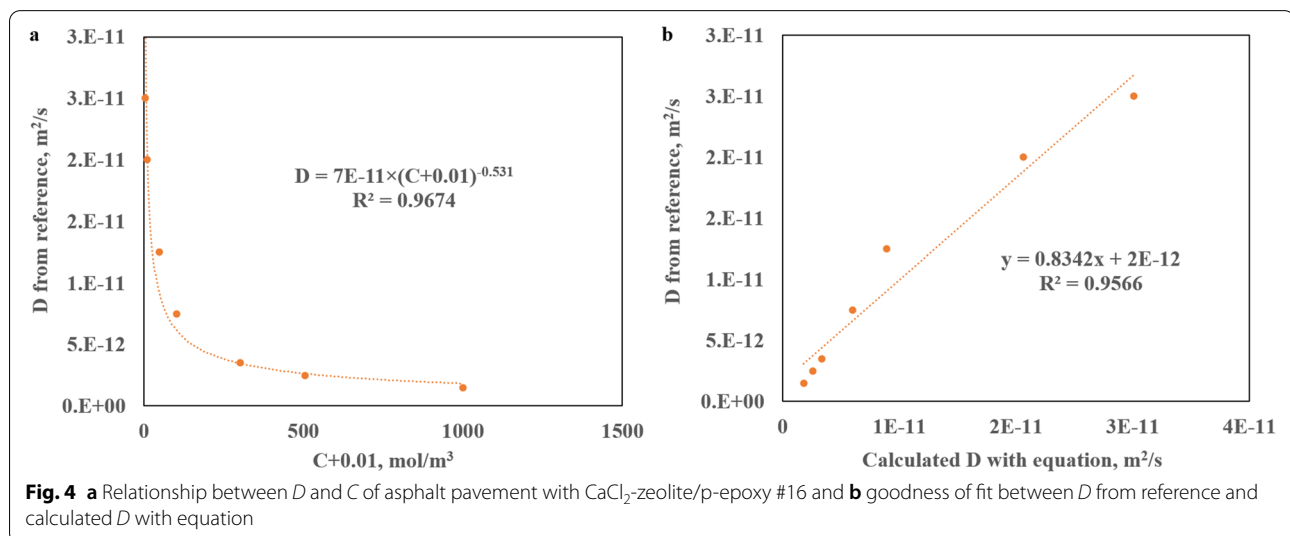
where $C(x, t)$ is the chloride concentration at a location x at a time t , C_s is the chloride concentration at surface, C_0 is the initial chloride concentration at location x , $\operatorname{erf}(z)$ represents the error function:

$$\operatorname{erf}(z) = \text{errorfunction} = \frac{2}{\sqrt{\pi}} \int_0^z e^{-y^2} dy \quad (18)$$

Thus, a steady-state chloride diffusion coefficient (D_{ss}) in asphalt mastic with a certain C_s at a given temperature can be estimated with Eqs. 17 and 18 incorporating a mastic diffusion test, which will be described in the Sect. 4.2.

In reality, the D of asphalt pavement is non-steady-state due to the variations of pavement temperature, chloride concentration, the depth, width, and number of thermal cracks and fatigue cracks, which have been considered in the model for more accurate results.

A previous study [37] reported that the D of cement concrete nonlinearly decreases with increasing the square root of C . The plot of the relationship between D and $(C+0.01 \text{ mol/m}^3)$ of cement concrete with a water-cement ratio of 0.6 is shown in Fig. 4, which was used to represent the relationship between D and C of the studied asphalt overlay, considering their comparable level of chloride diffusivity. A negligibly low background concentration of chloride, 0.01 mol/m^3 , was introduced to represent chlorides potentially sourced from aggregates and binder, aimed to avoid the non-converged calculation



in COMSOL Multiphysics. The water-cement ratio of 0.6 was selected because the D of this cement concrete was the closest to the D of asphalt mixture with 5.1 wt% CaCl_2 -zeolite/p-epoxy #16 [6, 29, 40, 52]. C -related coefficient to D (A_c) is expressed as:

$$A_c = \left(\frac{C + 0.01}{C_s} \right)^{-0.531} \quad (19)$$

where C_s is the surface chloride concentration used in the mastic diffusion test.

Pavement temperature also has significant influence on D . The effect of pavement temperature on D can be well expressed by the Arrhenius equation [50]:

$$D = D_0 \cdot \exp\left(-\frac{E_a}{RT}\right) \quad (20)$$

where D_0 is maximal diffusion coefficient, E_a is activation energy for diffusion, R is the universal gas constant, and T is the absolute temperature of asphalt pavement. According to [30], the D and T of cement concrete with a water-cement ratio of 0.6 had the relationship as shown in Fig. 5, which can be used for the relationship between D and T of asphalt pavement. Therefore, T -related coefficient to D (A_T) is expressed as:

$$A_T = e^{(4008.5 \times (-\frac{1}{T} + \frac{1}{T_t}))} \quad (21)$$

where T_t is the testing temperature of the mastic diffusion test.

The hourly data of pavement temperature T from May 1, 2012 to November 27, 2020 was calculated with Eq. 22

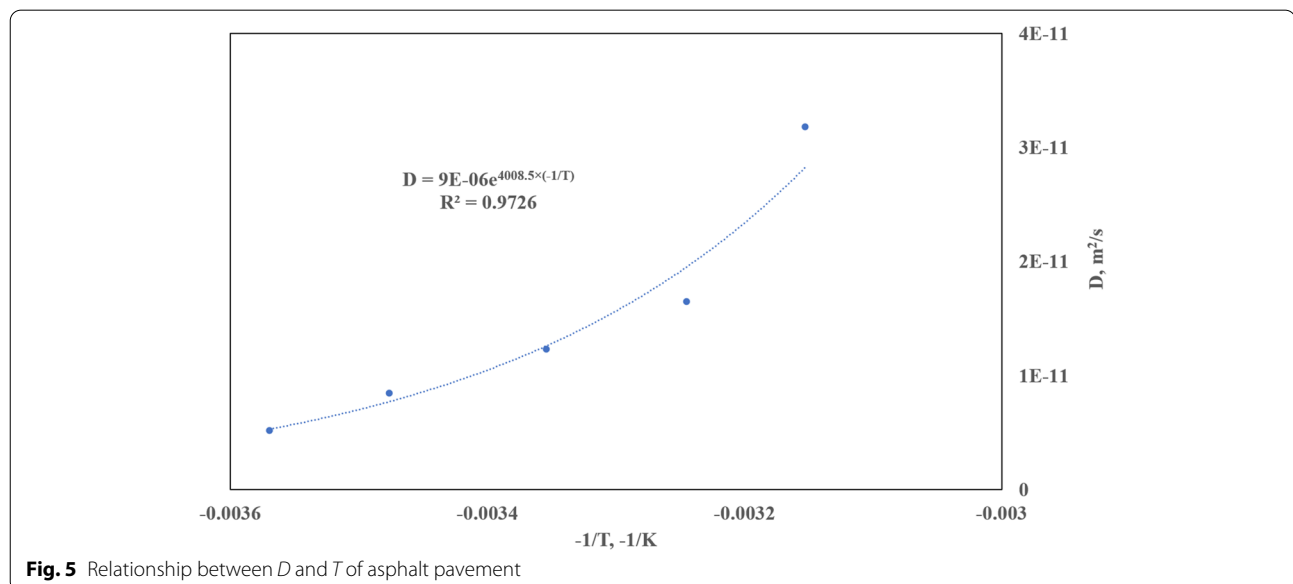
adapted from [15], and it was implemented using the “Interpolation” function of COMSOL Multiphysics.

$$T = 0.686 \times T_a + 0.000567 \times R_s - 27.87 \times d + 2.7875 \quad (22)$$

where T_a is air temperature, R_s is daily solar radiation, and d is depth from pavement surface. Arguably the functional pavement might retain more moisture than conventional asphalt pavement and thus feature a slightly different relationship than Eq. (22); but this difference is not considered at this stage of the modeling study.

Moreover, the initiation and propagation of the cracks in cement concrete are known to increase D [8, 12, 45]. In this study, considering the location (Pullman, WA), one can assume that thermal cracking and fatigue cracking were the dominant mechanisms for the development of cracking in the overlay over time. Other risks, such as rutting, raveling, stripping, alligator cracking, were not considered. Similar to cracked cement concrete, the thermal cracks and fatigue cracks in asphalt pavement increase D as well. The thermal cracking mainly results from low temperature environments, while the fatigue cracking is caused by repeated traffic loadings at moderate ambient temperatures.

There is no study reporting how D evolves in asphalt pavement over time as a function of thermal cracking or the relationship between D and the level of thermal cracking. To determine the D -time relationship under the effect of thermal cracking in asphalt pavement, a physical simulation was conducted using COMSOL Multiphysics incorporating a set of thermal cracking-time data adapted from Fig. 13 [14]. Four data points were



the thermal cracking percentage of the asphalt pavement was 0% (0 year), 27% (4 years), 38% (9 years), and 59% (11 years) were selected from [14] for this study. According to the definition of the thermal cracking percentage in the reference, the number of the cracks per 150 m length of the survey section was 0, 13.5, 19, and 29.5 corresponding to 0%, 27%, 38%, and 59%, respectively. For a 150 mm length overlay, the number of cracks at 0%, 27%, 38%, and 59% was 0, 0.0135, 0.019, and 0.0295 respectively. In other words, the corresponding number of the 150-mm section per crack was 0, 74, 53, and 34, respectively. To estimate D at different thermal cracking levels, the variation of the average C (C_{ave}) at the bottom of the simulation geometries over time was first determined with Eq. 23:

$$C_{ave} = \frac{N_n \times C_n + N_c \times C_c}{N_n + N_c} \quad (23)$$

where N_n is the number of the non-cracking 150-mm section, C_n is the chloride concentration at the bottom of the geometry of a non-cracking 150-mm section, N_c is the number of the 1-crack 150-mm section, and C_c is the chloride concentration at the bottom of the geometry of a 1-crack 150-mm section. C_n and C_c can be obtained from the simulation described below.

Figure 6 shows the geometries used to determine C_n and C_c in COMSOL Multiphysics. The geometry in Fig. 6a is the same as the geometry used in the Sect. 3.1. The geometries in Fig. 6b-d include inverted triangle cracks with different depths and widths. The circles in the geometry were used as traditional aggregates instead of the additive. For simplicity, the model had the following assumptions:

1. the max crack depth of the overlay was 30 mm at 59%;
2. the max crack width was half of the max crack depth;
3. the ratio of two max crack depths was proportional to the ratio of the two thermal cracking percentages.

In the “tds” interface, the aggregates were excluded from computing. The D_{ss} in asphalt mastic had been determined with the mastic diffusion test. It was assumed that the initial value of the chloride concentration in the asphalt mastic was 0. The C_s on the top and crack surfaces of the geometry was 560 mol/m³. The output was the relationship between the chloride concentration (e.g., C_n and C_c) at the bottom of the geometry and time. Eleven points were selected to calculate C_n and C_c over time. The simulated C_{ave} over time at each cracking level was determined with Eq. 23. Meanwhile, the chloride transport follows the Fick’s second law. Thus, D at each cracking level was estimated where the C-time curve calculated according to Eqs. 17 and 18 matched best with the C_{ave} -time curve simulated with COMSOL Multiphysics. Figures S6, S7, S8 and S9 show the simulated and calculated C-time curves and the goodness of fit at different cracking levels. The D-time relationship related to thermal cracking is shown in Fig. 7. Therefore, thermal cracking-related coefficient to D (A_{tc}) is expressed as:

$$A_{tc} = e^{(2E-10) \times t} \quad (24)$$

The fatigue cracking-related coefficient to D (A_{fc}) was determined with the same method of A_{tc} . The datapoints of equivalent single axle loads (ESALs) and crack properties (e.g., crack rate and crack width) used for this study were adapted from [21]. Lane #9 was a 90-mm asphalt layer constructed on a 153-mm in-place stabilized soil cement (10%) subbase under a 102-mm layer of crushed stone. The relationship between ESALs and crack rate is shown in Figure S10, which was adapted according to the curve of Lane #9 in Fig. 7.2 in the main text of a reference [21]. The ESALs-crack width relationship as shown in Figure S11 was obtained based on Figures S12 and S13, which were adapted according to the figure of the sample No.25 with a load of 7.25 KN in Appendix D of the reference [21] and the single load equivalency factor (LEF) data of a design guide (Transportation Officials, 1993) respectively. The crack width-crack depth relationship

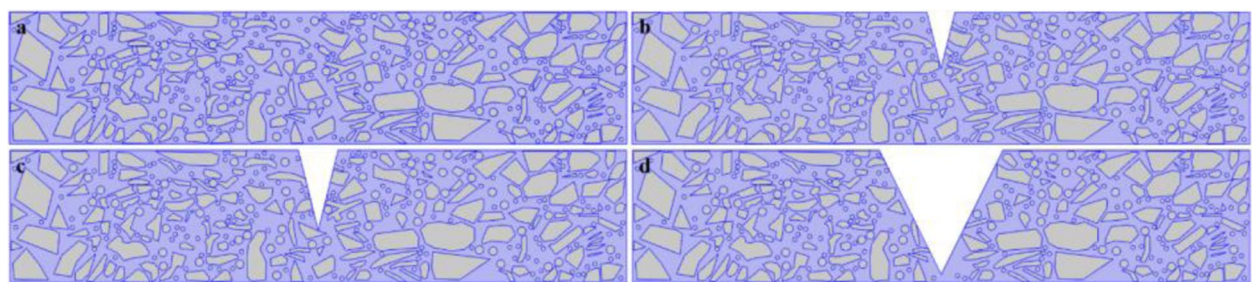


Fig. 6 COMSOL geometries used to determine C_n and C_c related to thermal cracking of asphalt pavement. **a** 0% cracking, **b** 27% cracking, **c** 38% cracking, and **d** 59% cracking

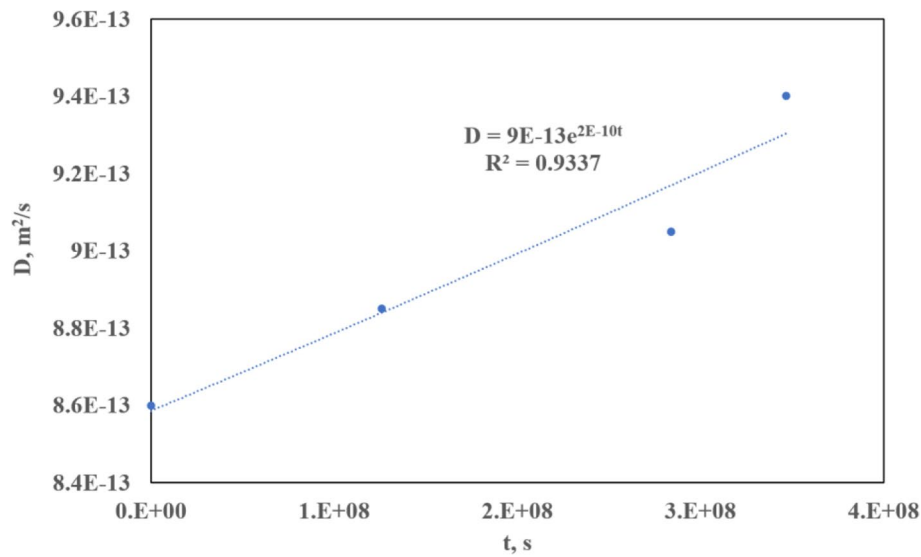


Fig. 7 D-time relationship related to thermal cracking

as shown in Figure S14 was adapted from Fig. 5.22 of a reference [21]. The time-ESALs datapoints at State Route 195 near Pullman in Washington State from 2010 to 2019 as shown in Table S4 were obtained from the long-term pavement performance (LTPP) program of Federal Highway Administration, United States Department of Transportation.

It was assumed that the lane width of the 150 mm-section model was 3.66 m and all fatigue cracks were transverse fatigue cracks. According to the equation in Figure S10, Table S4, and Eq. 25, the length of the transverse fatigue crack (L) in a 150 mm-section model was determined. L then was converted to the number of 150-mm sections at different years when one transverse fatigue crack existed and crossed the whole lane of the model, as shown in Table S5. The width of the transverse fatigue crack was determined according to the equation in Figure S11, and the total depth of the transverse fatigue crack was determined according to the equation

in Figure S14. It was assumed that the transverse fatigue crack started cracking from the bottom of a 50-mm binder course under the overlay. Thus, the depth of the transverse fatigue crack in the model was calculated using the total depth minus 50 mm. The depth and the width of the transverse fatigue crack are shown in Table S6. In COMSOL Multiphysics, the geometries used to determine C_n and C_c related to the fatigue cracking of asphalt pavement are shown in Fig. 8. The settings in the “tds” interface for fatigue cracking and the calculating procedures were similar with that for thermal cracking.

$$L = \text{pavementsurfacearea} \times \text{fatiguecrackrate} \quad (25)$$

Figures S15, S16, S17 and S18 show the simulated and calculated C-time curves and the goodness of fit at different years for fatigue cracking. The D-time relationship related to fatigue cracking is shown in Fig. 9. Therefore, A_{fc} is expressed as:

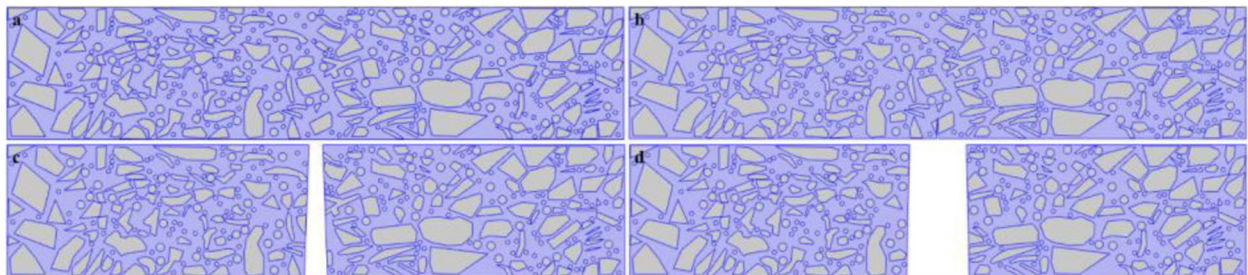
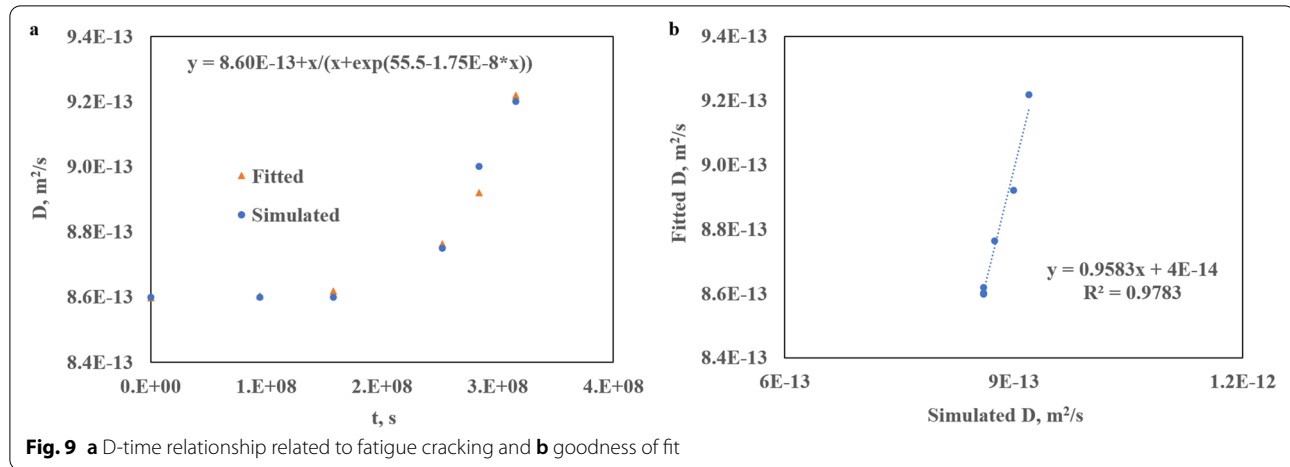


Fig. 8 COMSOL geometries used to determine C_n and C_c related to fatigue cracking of asphalt pavement. **a** 0 year, **b** 8 years, **c** 9 years, and **d** 10 years

**Table 2** Parameters related to D_{mastic} in the model

Parameter	Value/Equation	Unit
D_{ss}	$1.14E-12$	m^2/s
C_s	560	mol/m^3
A_C	$((C + 0.01)/C_s)^{-0.531}$	NA
T_t	288.15	K
A_T	$EXP(4008.5 \times (-1/T + 1/T_t))$	NA
A_{tc}	$EXP((2E-10) \times t)$	NA
A_{fc}	$1 + t/((8.6E-13) \times (t + EXP(55.5 - (1.75E-8) \times t)))$	NA
D_{mastic} when $s_1 \geq 0.2$	$D_{ss} \times A_C \times A_T \times A_{tc} \times A_{fc}$	m^2/s
D_{mastic} when $s_1 < 0.2$	0	m^2/s

T Temperature in K; NA Not Applicable

$$A_{fc} = 1 + \frac{t}{(8.6E - 13) \times (t + e^{55.5 - (1.75E - 8) \times t})} \quad (26)$$

Combining D_{ss} , Eq. 19, Eq. 21, Eq. 24, and Eq. 26, the final equation for the D of asphalt mastic (D_{mastic}) in the tds interface was expressed as:

$$D_{mastic} = D_{ss} \times A_C \times A_T \times A_{tc} \times A_{fc} \quad (27)$$

In addition, the threshold of moisture volume fraction (s_1) in concrete for chloride diffusion was 20% [35]. As such, D_{mastic} was expressed as Eq. 27 when s_1 was equal or greater than 0.2, while D_{mastic} was 0 when s_1 was less than 0.2, in which s_1 was the result of the “phtr” interface.

The parameters related to D_{mastic} mentioned above are provided in Table 2.

Transport properties of additives

The D in the additives in the presence of water ($D_{additive}$) was estimated with the cooperation of the curve of

chloride concentration vs. time in water from an additive immersion test and the curve of chloride concentration vs. time in water simulated with the tds interface of COMSOL Multiphysics. $D_{additive}$ was determined when the two curves had the best fit. The additive immersion test is described in the Sect. 4.2.

In the “tds” interface, the geometry used to simulate the C-time curve and the original image of the layer of the compacted asphalt-coated additives in the beaker for the test are shown in Fig. 10a and b, respectively. The total height and the width of the geometry were 132.5 mm and 120 mm respectively, which were the height and the width of the water in the beaker. In the geometry, the gray part is water and the rest represent the compacted asphalt-coated additives with a height of 17.5 mm, which was pictured using AutoCAD according to Fig. 10c. Figure 10c was the processed image according to Fig. 10b using ImageJ.

In the settings of transport properties, $D_{additive}$ was a value that needed to be solved to achieve the best match between the experimental vs. simulated chloride concentration curves, and the D in water was $1.2E-9 m^2/s$ derived from the reference [13]. The initial value of the C in water was 0, and the initial value of the C in the additives ($C_{initial}$) was another value to be solved for a match between two chloride concentration curves.

The simulation output was the simulated C-time curve. Simulation results showed the two curves (Figure S19) had the best match when $D_{additive}$ was $2E-11 m^2/s$ and $C_{initial}$ was $1500 mol/m^3$. The data points before 71 h in Figure S19b were removed due to the unstable diffusion at the very early stage of the test. Same as the expression of D_{mastic} , $D_{additive}$ was affected by s_1 from the result of the “phtr” interface. $D_{additive}$ was equal to $2E-11 m^2/s$ when s_1 was equal or greater than 0.2, while $D_{additive}$ was 0 when s_1 was less than 0.2.

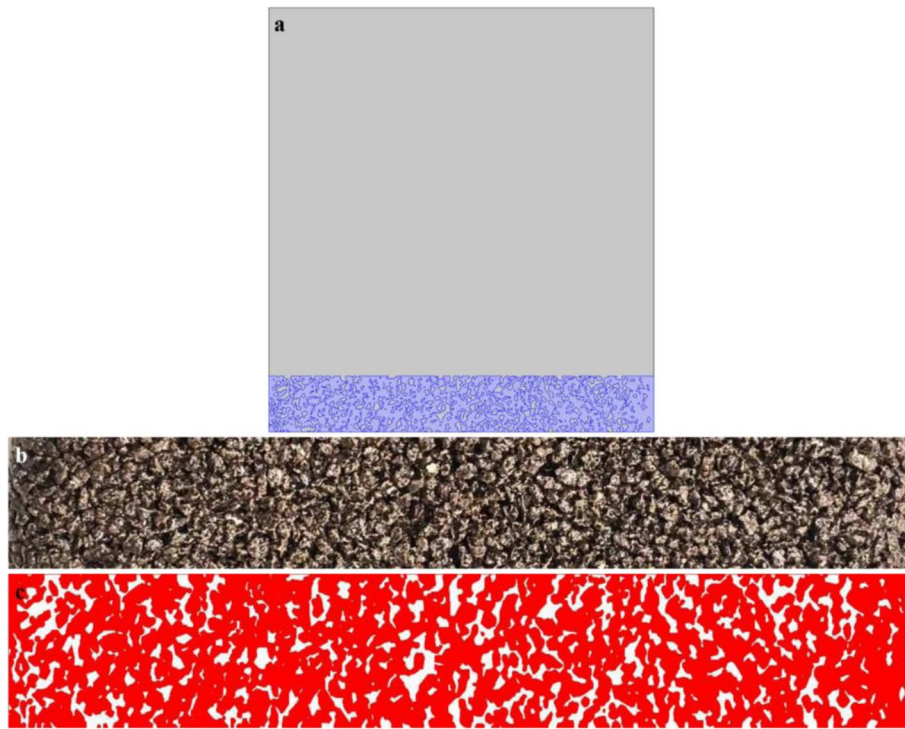


Fig. 10 **a** Geometry used to simulate the C -time curve, **b** original image of compacted asphalt-coated additives, and **c** processed image of compacted asphalt-coated additives with ImageJ

Initial values and boundary conditions

In reality, CaCl_2 exists in a liquid state when water is sufficient, otherwise it is in a solid state. The C in the additives was supposed to be affected by s_1 from the water transport model as well, but this effect was difficult to be simulated in COMSOL Multiphysics at this stage. As such, this study assumed that in a very short time the C in the additives reached to the maximum value (7325 mol/m^3), which was calculated based on the average volume of the additives. For simplicity, the amount of available water within the sphere of influence of the additives was assumed to be equivalent to the volume of the additives. Subsequently, the C in the additives decreased over time until the system reached a balanced C . To this end, the initial value of the C in the additives in the model was set to be 7325 mol/m^3 , while the initial value of the C in the asphalt mastic was assumed to be 0 mol/m^3 .

The C in asphalt mastic and on the top surface of the overlay may gradually increase over time until it reaches to the maximum C . In the service environment, part of the salt on overlay surface is washed away by rainfalls and snowfalls. There is no study reporting how much of the salt is removed by rainfalls or snowfalls. Based on field observations, this study assumes that approximate 5% and 50% of the C on the top surface of the overlay

remained after the hour of rainfall and snowfall, respectively. The boundary condition related to C on the top surface of the geometry was implemented by the functions of “Flux” and “Interpolation” in COMSOL Multiphysics. The snowfall season was defined as from November 13 to February 25 every year in Pullman, Washington.

Figure 11 shows the flowchart of the water transport model, the chloride transport model, and how the output of the water transport model affects the chloride transport model.

Mesh and study

The asphalt mastic, additives, and top surface boundary were meshed according to their sizes. The free triangular mesh was selected as the mesh of the model. This study selected the normal size, fine size, and finer size of mesh for the asphalt mastic, additives, and top surface boundary, respectively.

Both the water transport time-dependent model and the chloride transport time-dependent model were studied for 44,280 h (approximate 5.05 years) with an interval of 1 h. This is because in practice such an overlay would be replaced after 5 years in service and some of the model assumptions would no longer hold true if the asphalt

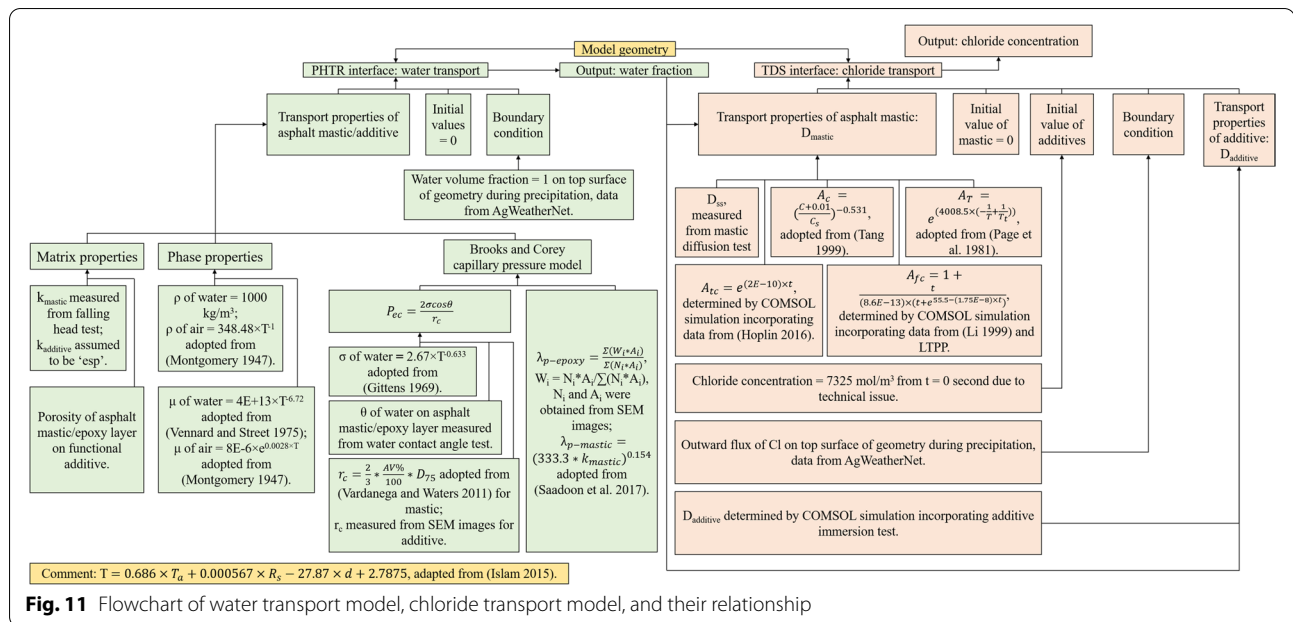


Fig. 11 Flowchart of water transport model, chloride transport model, and their relationship

overlay serves beyond 5 years in the field where moisture damage, UV aging, etc. start to notably compromise the integrity of the overlay.

Experimental

Materials

In this study, the same materials including asphalt binder and aggregates less than 4.75 mm, the same mixing design, and the same mixing and compaction procedure as in our previous study [53] were used to prepare asphalt mastic. The aggregates greater than 4.75 mm were not included in asphalt mastic. The air void of the asphalt mastic samples was $7\% \pm 0.5\%$.

The same fabrication procedure and materials including CaCl_2 , zeolite, epoxy, halloysite nanoclay, and acetone as in our previous study [53] were used to prepare CaCl_2 -zeolite/p-epoxy #16. The calculated density of CaCl_2 -zeolite/p-epoxy #16 is 1.98 g/cm^3 .

Calcium nitrate tetrahydrate ($\text{Ca}(\text{NO}_3)_2 \cdot 6\text{H}_2\text{O}$) was purchased from Thermo Fisher Scientific.

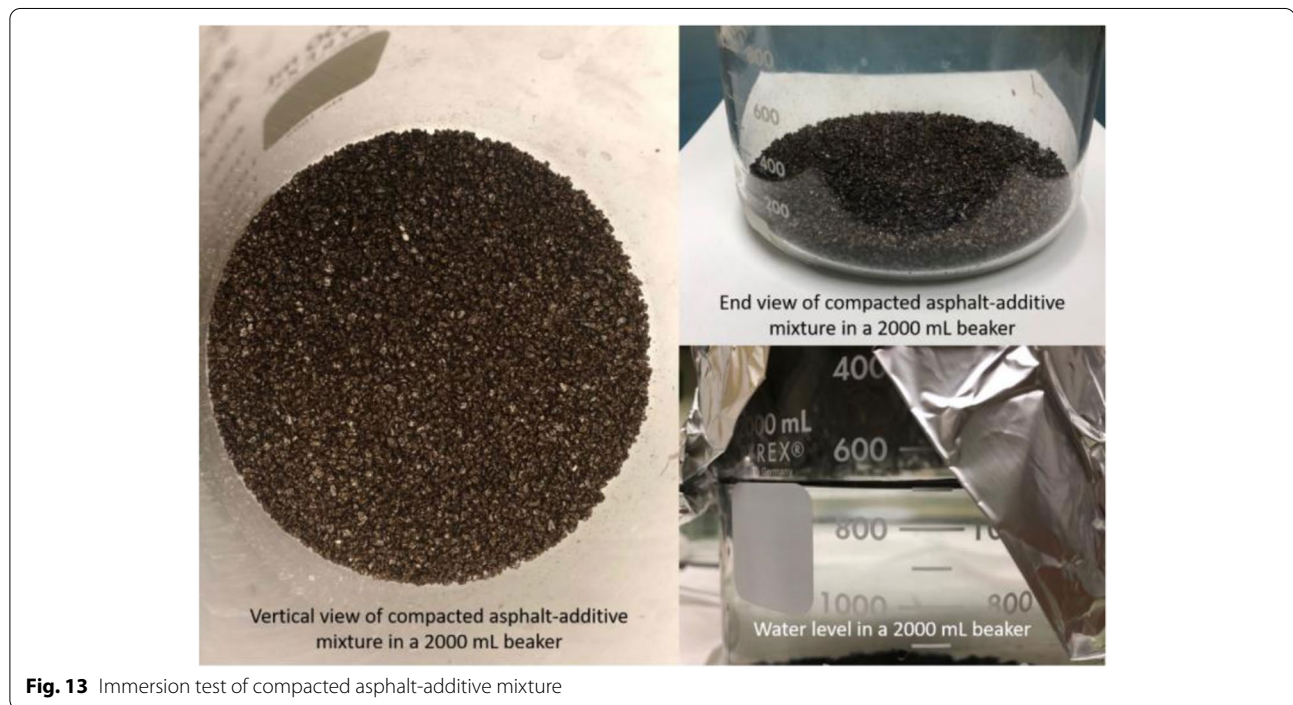
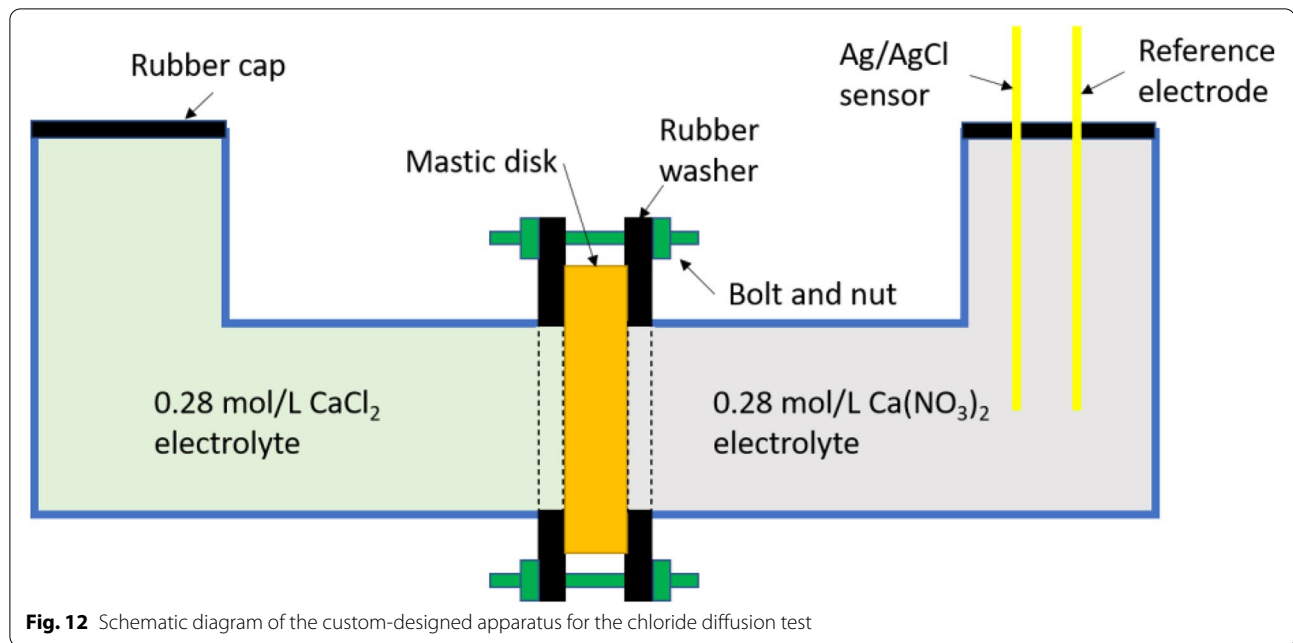
Testing methods

To evaluate the diffusion behavior of chloride ions in asphalt mastic, a mastic diffusion test was adopted with a custom-designed apparatus as shown in Fig. 12. A mastic disk was sandwiched between two plastic cells, which were used to store the electrolyte solutions of CaCl_2 and $\text{Ca}(\text{NO}_3)_2$, without any leakage. Mastic disk samples with a thickness of $12 \text{ mm} \pm 0.5 \text{ mm}$ were cut from the prepared asphalt mastic samples and polished with sandpapers. The two cells were filled with DI water

to saturate the mastic disk samples for 24 h before the mastic diffusion test, to minimize the effect of wick action (water transport) during ionic penetration [22]. Then, DI water was replaced by 0.28 mol/L (3 wt%) CaCl_2 electrolyte solution in the left cell and 0.28 mol/L $\text{Ca}(\text{NO}_3)_2$ electrolyte solution in the right cell. To avoid the evaporation of the water, the cells were covered by rubber caps. The variation of the chloride concentration over time in the right cell was periodically measured using a laboratory-prepared Ag/AgCl chloride sensor, which has been calibrated using standard NaCl solutions before each of measurements. The testing temperatures were 15°C . The results of the test are shown in Figure S20. It is assumed that the D has been stable at the last point of the curve in Figure S20b, therefore D_{ss} was equal to $1.14\text{E-}12 \text{ m}^2/\text{s}$.

The inside-to-outside diffusion of chloride ions in CaCl_2 -zeolite/p-epoxy #16 was investigated by an additive immersion test, in which the manually compacted mixture of 133.6 g CaCl_2 -zeolite/p-epoxy #16 and 7.2 g asphalt (5.1 wt% binder content) was soaked in 1.5 L DI water at 15°C as shown in Fig. 13. The mixing temperature was 145°C , and the porosity of the mixture was 40%. The chloride concentration was monitored periodically by the same method used in the mastic diffusion test.

A falling head test [1], which is suitable for dense asphalt mixture samples with a low permeability, was used to evaluate k_{mastic} . Figure 14 shows the schematic diagram of the setup of the falling head test. The diameter and thickness of mastic disk samples for the falling



head test were $58 \text{ mm} \pm 0.5 \text{ mm}$ and $12 \text{ mm} \pm 0.5 \text{ mm}$. The asphalt mastic samples were saturated for 24 h before the test. The upper and lower levels of water in the standpipe, the volume of water passing through a sample, and the time required for the water passing through the sample were measured. The equations used

to calculate k_{mastic} are expressed as Eqs. 28 and 29. The parameters and results of the test is shown in Table S7.

$$K_{\text{mastic}} = \frac{A_2 \times L_s \times \ln\left(\frac{H_1}{H_2}\right)}{A_1 \times t} \quad (28)$$

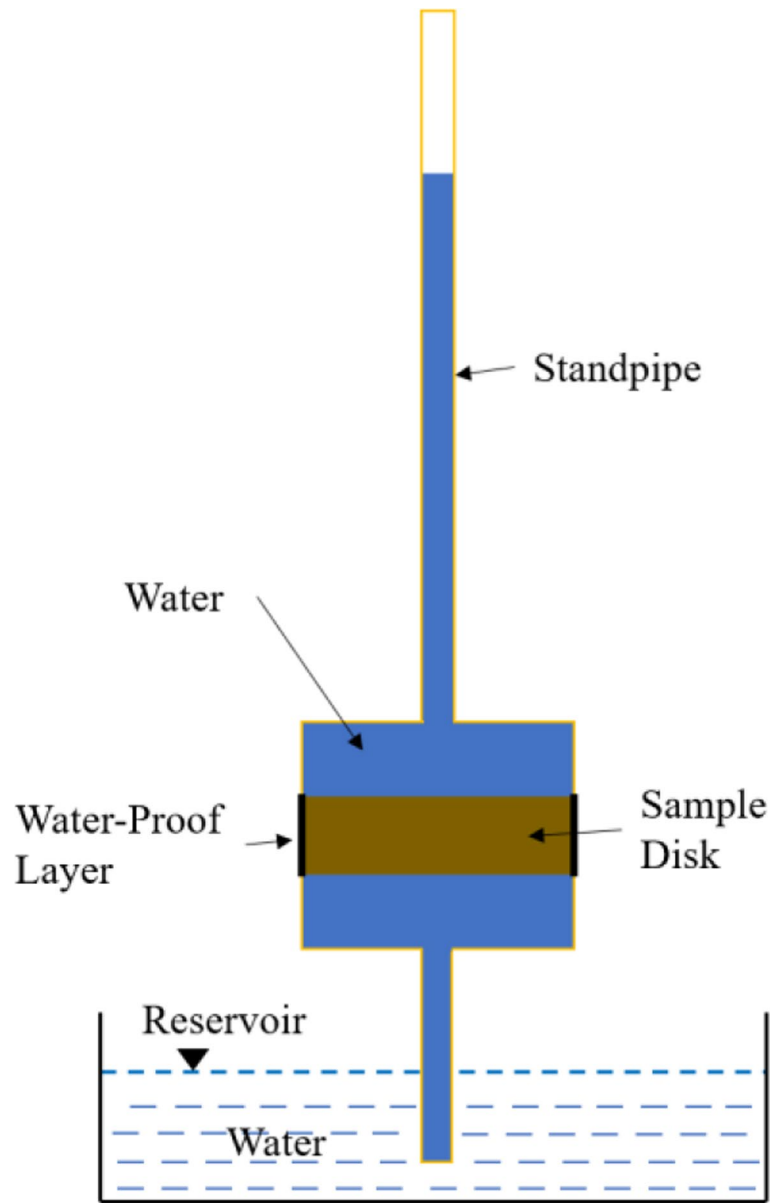


Fig. 14 Setup of the falling head test

where K_{mastic} is the hydraulic conductivity of asphalt mastic, H_1 is the initial height of water in standpipe, H_2 is the final height of water in standpipe, A_1 is the cross-sectional area of sample, A_2 is the cross-sectional area of standpipe, L_s is the length of sample, and t is the elapsed time of test.

$$k_{\text{mastic}} = \frac{K \times \mu_w}{\rho_w \times g} \quad (29)$$

where μ_w is the dynamic viscosity of water at 25 °C, ρ_w is the density of water, and g is the gravitational acceleration.

Water contact angle test was used to measure the values of θ of water to the epoxy layer and the asphalt mastic. An example of water contact angle tests on asphalt mastic is shown in Fig. 15. The results of the water contact angle test are shown in Table S8.

SEM (JEOL JXA8500F Field Emission Electron Microprobe) was adopted to measure the radii



Fig. 15 Representative water contact angle test on asphalt mastic

of the micropores in the epoxy coating layer of CaCl_2 -zeolite/p-epoxy. More details can be found in our previous study [53].

Results and discussion

Water transport

Figures 16, 17, and 18 depict the simulation results of the water transport model. Figure 16a–16f display the representative images of the evolution of the s_1 in the

overlay when exposed to varying precipitation and temperature. At the very beginning (Fig. 16a, $t=0$ h), the s_1 regardless of the location was in the model was equal to 0 because there was no rainfall or snowfall on the overlay. At 72 h (Fig. 16b), the s_1 increased to different levels, depending on the location in the model. Two rainfalls between 0 and 72 h accounted for the increase in the s_1 , which could be observed in Fig. 17. Figure 17a illustrates the temporal evolution of the s_1

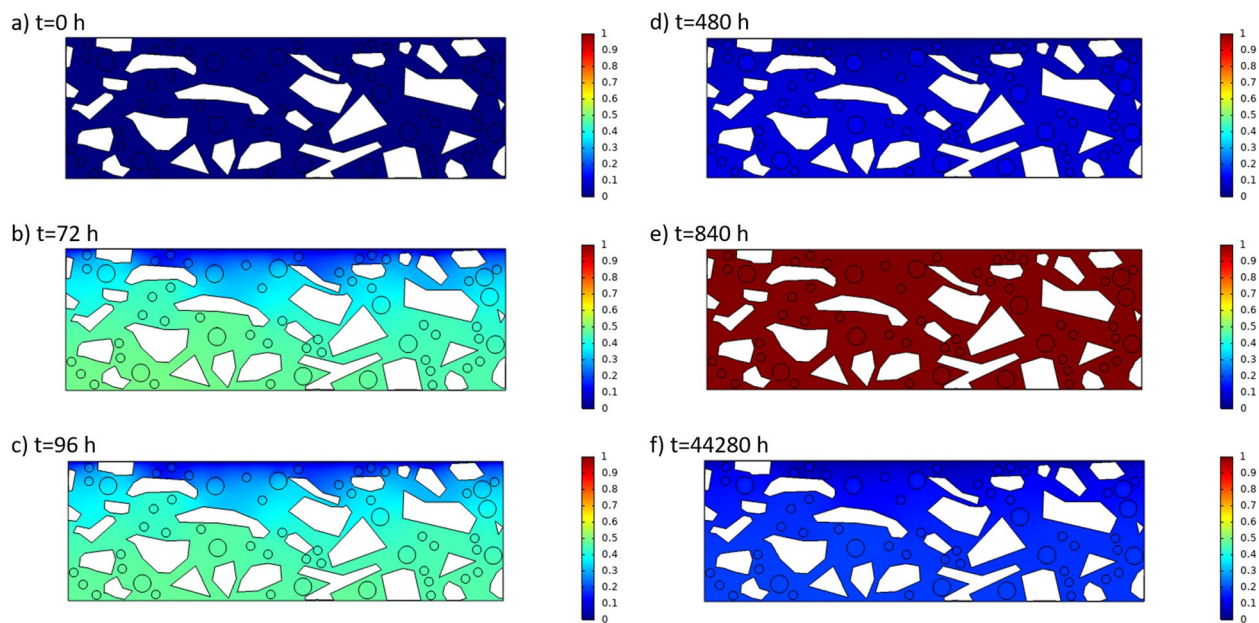


Fig. 16 Representative images of evolution of s_1 in APSSA when exposed to variations of precipitation and temperature. From a to f, $t = 0, 72, 96, 480, 840, \text{ and } 44,280$ h respectively

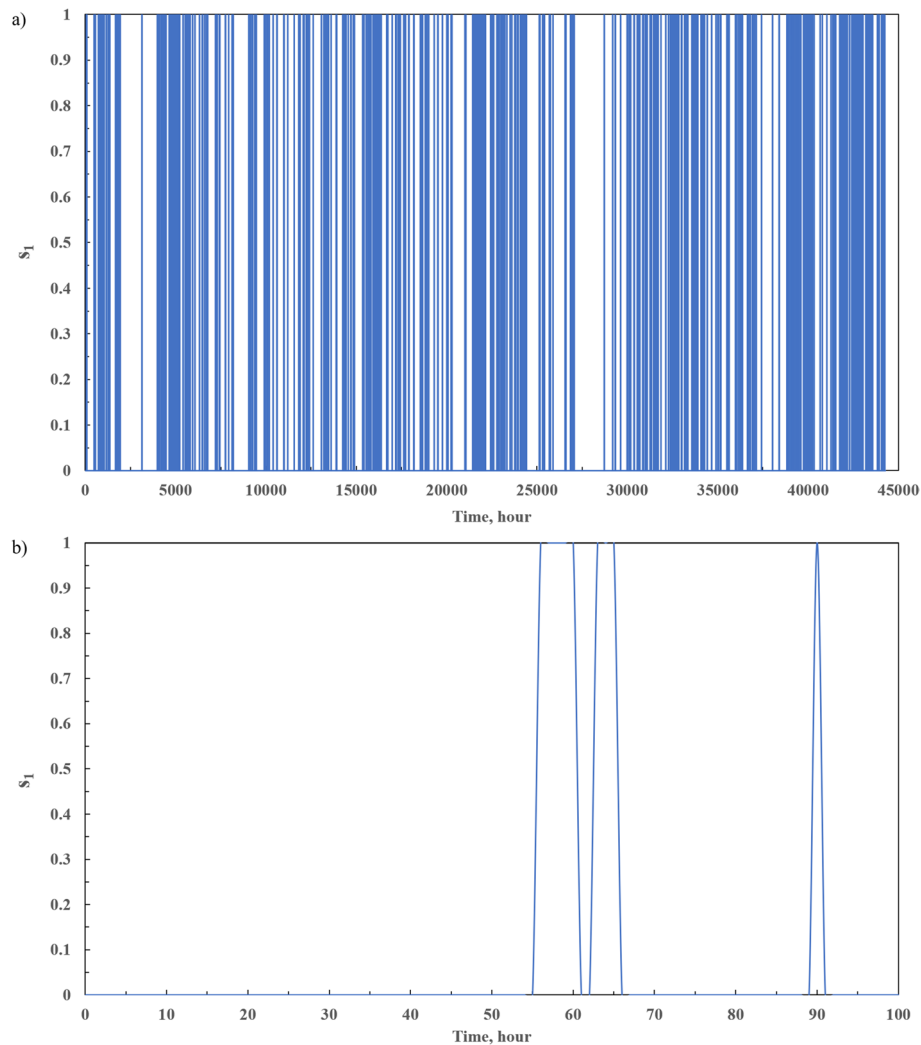


Fig. 17 s_1 on top surface. **a** full-scale figure and **b** local enlarged figure

on the top surface of the overlay up to 44,280 h. To see the lines clearly, a local enlarged figure (Fig. 17b) up to 100 h was plotted. Figure 17b reveals that the first rainfall appeared between 56 and 60 h and the second one rained between 63 to 65 h. In contrast, the drying process between 60 and 63 h and after 65 h was responsible for the different values of the s_1 at the different locations. Water could only evaporate through the top surface, which explains why the s_1 near the top surface had lower values than that around the middle and the bottom. At 96 h (Fig. 16c), the s_1 changed slightly due to the corporation of the third 1- hour rainfall (as shown in Fig. 17b) and the drying process after 90 h. Between 96 and 480 h, there was no rainfall. Therefore, the s_1 gradually decreased to low values over time, as shown

in Fig. 16d. Figure 16e reveals that all the s_1 in the overlay reached to 1 at 840 h, resulting from sufficient amount of rains falling on the surface before 840 h. The last status of the overlay about s_1 for this study was shown in Fig. 16f (44,280 h, about 5.05 years). Figure 18 illustrates the temporal evolution of the s_1 at the center of the geometry (in asphalt mastic), which was consistent with the results shown in Figs. 16 and 17.

It should be noted that pavement temperature is a variable in several equations of the model's inputs, including the entry capillary pressure of water in pores of asphalt mastic and functional additive, the dynamic viscosity of water and air, and the density of air. Pavement temperature affects the water fraction through influencing these parameters.

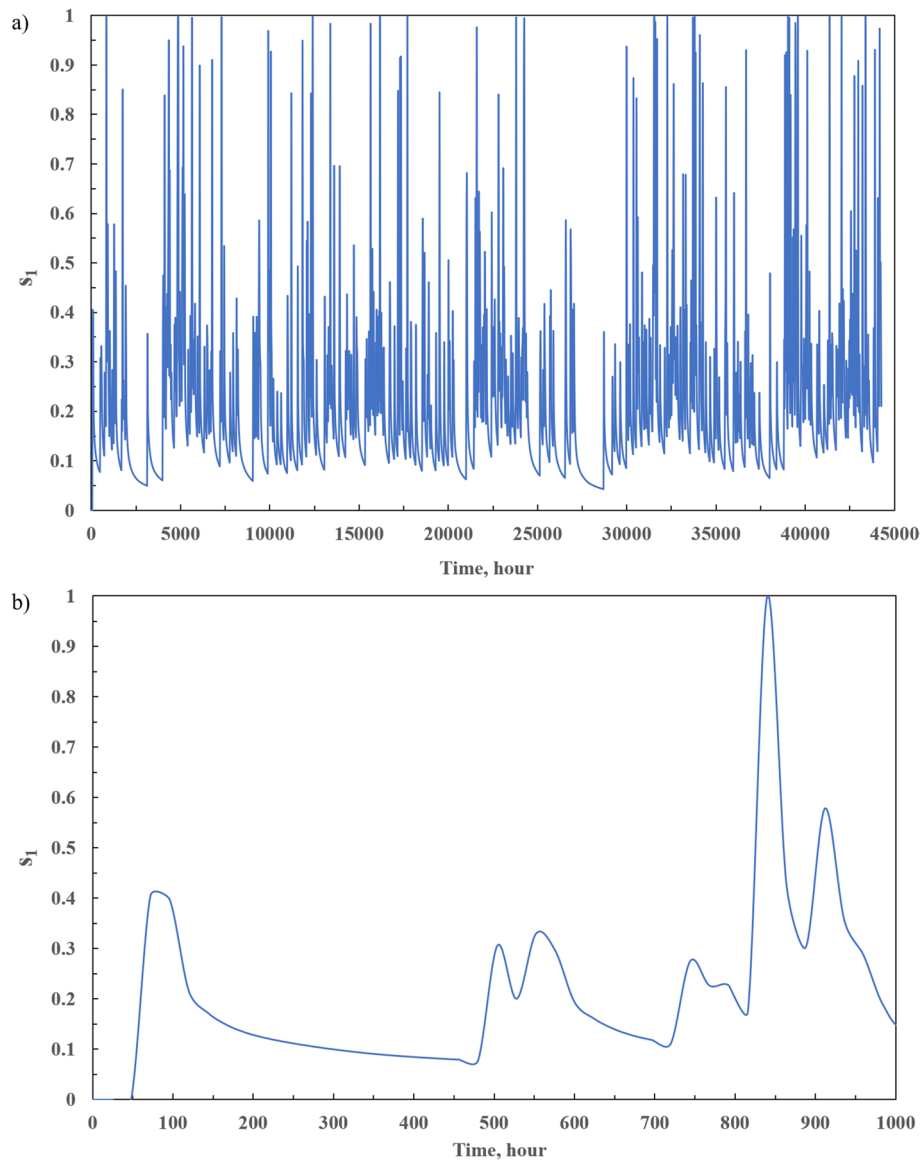


Fig. 18 s_1 at center of geometry. **a** full-scale figure and **b** local enlarged figure

Chloride Transport

Figure 19 displays the representative images that illustrate the temporal evolution of the C in the overlay when exposed to wet-dry cycles, varying pavement temperature, pavement thermal cracking, and pavement fatigue cracking. The wet-dry cycles in the model were expressed by s_1 (≥ 0.2 for a wet condition and < 0.2 for a dry condition), which resulted from the prediction of the water transport model. The C in asphalt mastic was 0 mol/m^3 from 0 to 48 h as shown in Fig. 19a-c, because the overlay was in a dry condition ($s_1 < 0.2$) as shown in Fig. 17b. After the first rainfall, the s_1 in asphalt mastic was greater than 0.2, thus the C gradually increased over

time (as shown in Fig. 19d-f) until the s_1 decreased to be lower than 0.2 due to water evaporation (when there was no rainfall on the pavement). Figure 19f-h indicate that the C in asphalt mastic remained unchanged from 144 to 240 h. The reason was that the D_{mastic} was equal to 0 when the s_1 was lower than 0.2 during that period as shown in Fig. 18b. At 4272 h (Fig. 19i), the C in asphalt mastic greatly increased while the C in functional additives significantly decreased, relative to those before 240 h. Chloride ions in the overlay moved gradually from the locations with high concentrations to the locations with low concentrations. The last status of the C in asphalt mastic and functional additive for this study

was shown in Fig. 19j (44,280 h, about 5.05 years). In this figure, the C in asphalt mastic near the top surface (the blue area) was visibly lower than that at the middle and bottom, which is due to dilution and removal of chloride ions from the top surface by precipitation of rain or snow. The C at deeper areas has higher values, mainly because the chloride ions in the additives at deeper areas need to travel longer distances to reach the top surface and their transport takes more time than the time needed by the dilution.

In addition to moisture availability (due to precipitations), pavement temperature, pavement thermal cracking, and pavement fatigue cracking were three coefficients in the equation of the diffusion coefficient of asphalt mastic, all of which influenced the change of the C in asphalt mastic and functional additive accordingly.

Although Fig. 19 qualitatively illustrates the overall variation of the C in the overlay, it is desirable to quantitatively monitor the continuous evolution of the C in functional additive and asphalt mastic and on the top surface, respectively. Therefore, Figs. 20, 21, and 22 were plotted accordingly.

Figure 20 contrasts the temporal evolution of the C in three functional additives at three different locations: top, middle, and bottom. They all shared a same trend and gradually decreased over time. In some periods the curve of the C exhibited a stable plateau phase due to that the D_s of asphalt mastic and functional additive were $0 \text{ m}^2/\text{s}$ because the s_1 was equal to 0. The slight differences among the three C s resulted from the surrounding environment of the three additives, such as the quantity of functional additives and aggregates nearby, the shape of

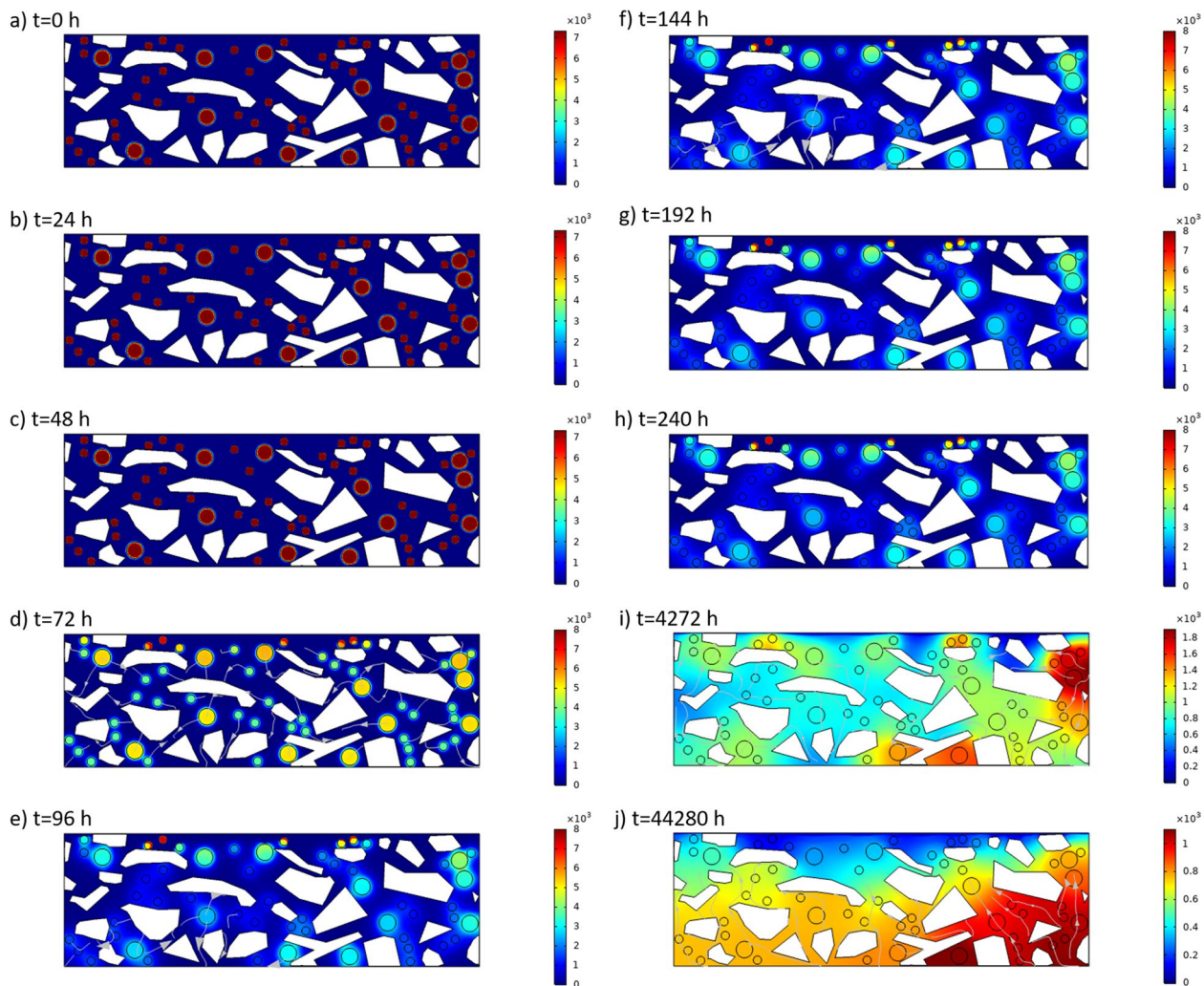


Fig. 19 Representative images of evolution of C in APSSA when exposed to wet-dry cycles and variations of temperature, pavement thermal cracking, and pavement fatigue cracking. From a to j, $t=0, 24, 72, 96, 144, 192, 240, 4272$, and $44,280 \text{ h}$ respectively

adjacent aggregates, and the cumulative time when s_1 was equal or greater than 0.2.

Figure 21 illustrates the temporal evolution of the C on the top surface of the overlay. Five points on the top surface were selected, and the averaged C was plotted. It can be seen that the C on the top surface was reduced following the pattern of precipitations shown in Fig. 17. The amount of the reduction in C depended on the type of precipitation; the reduction in C was not exact 95%

and 50% for rainfalls and snowfalls respectively. This is because that the setting in COMSOL Multiphysics for the chloride removal at top surface was the boundary condition 'Flux', instead of directly removing the available C . Arguably, the plot shown in Fig. 21 better represents the reality.

The effective anti-icing concentration of Cl^- in water for different temperatures is provided in Table 3, which was converted based on the phase diagram for the

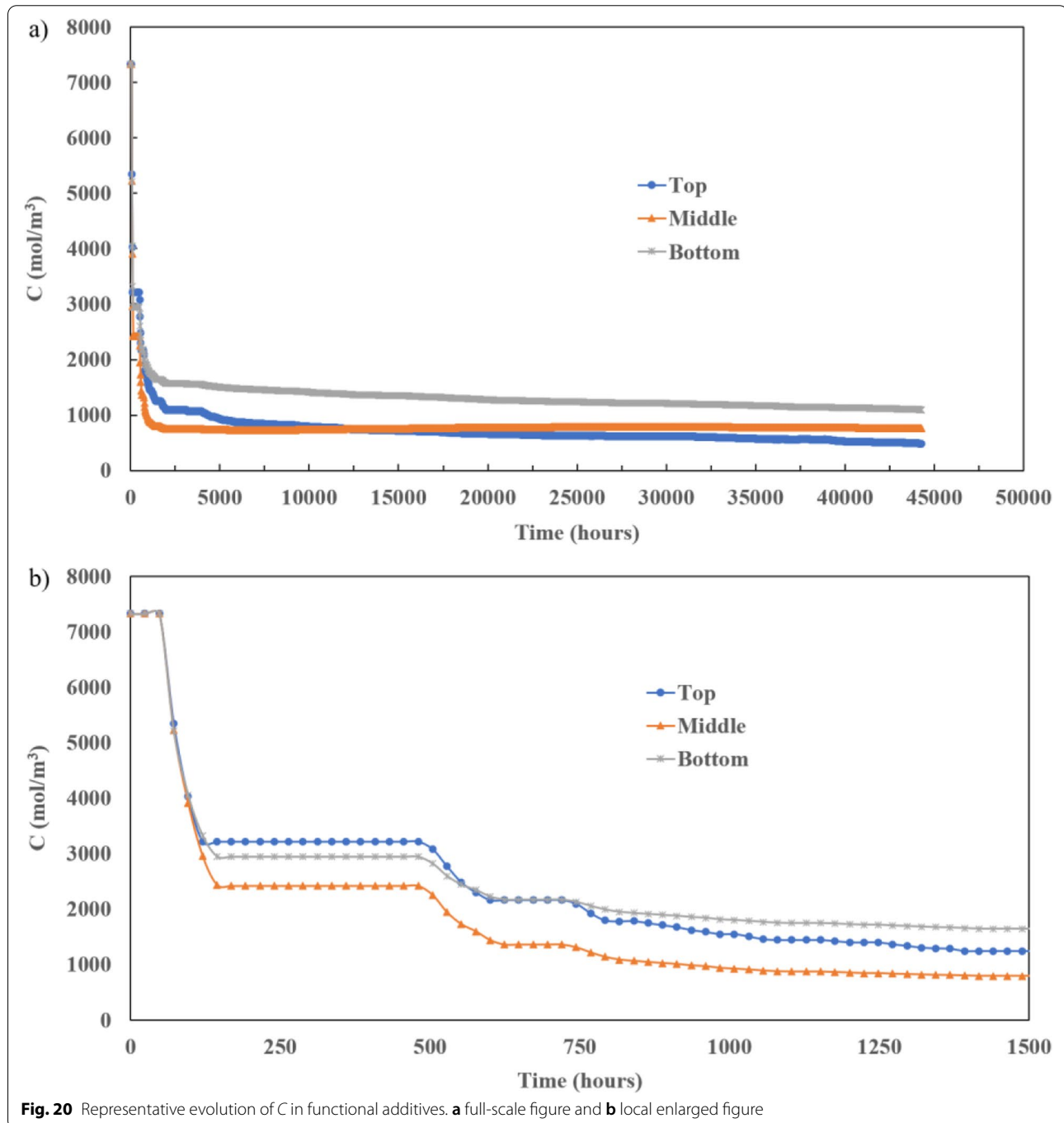


Fig. 20 Representative evolution of C in functional additives. **a** full-scale figure and **b** local enlarged figure

water- CaCl_2 system as shown in Figure S21. One can assume that there is a linear relationship between temperature and the CaCl_2 concentration (in wt%) when the temperature is higher than -10°C . The equation is expressed as:

$$C_{\text{CaCl}_2} = -\frac{1}{80} \times T \quad (30)$$

where C_{CaCl_2} is the effective mass percentage of CaCl_2 for anti-icing at T and T is temperature. The temperature of asphalt pavement near surface is usually 1 to 2°C higher than air temperature during winter [34], and snow events generally occur when air temperature is lower than 0°C in winter. As such, this study assumes that snow events occurred when the temperature of the overlay dropped below 2°C , and the historical hourly pavement temperature data (near Pullman, WA) below 2°C were thus used to calculate the statistical parameters (e.g., percentiles mentioned later).

Considering the compressed or vibrated pavement surface due to the effects of loading and friction from moving vehicles [54] and the average size of functional additive being 2 mm , this study assumes that the C in the overlay at a depth of 4 mm approximately determines whether the anti-icing function is effective or not. The averaged C of five points in asphalt mastic at the depth of 4 mm was plotted as shown in Fig. 22. At the beginning, the C increased rapidly and reached to $1,118\text{ mol/m}^3$

within two months. The fast diffusion resulted from the big difference of the C between asphalt mastic and functional additives. Subsequently, the C gradually decreased over time, due to chloride removal on the top surface. According to the plot in Fig. 22 and the data in Table 3, the anti-icing function of the overlay was fully effective in $17,520\text{ h}$ (2 years) and $43,800\text{ h}$ (5 years) for the minimum pavement temperature above -3.4°C and -2.4°C , corresponding to its lowest C of 808 mol/m^3 and 569 mol/m^3 , respectively. These two pavement temperatures translate to 97.4-percentile and 96.3-percentile of historical hourly pavement temperature near Pullman, Washington, respectively. In other words, this specific 16-mm thick functional overlay could prevent the surface from icing, for 97.4% of the snow events within 2 years and for 96.3% of the snow events within 5 years. The simulation results agree well with the estimated anti-icing life using Eq. 3.2 in our previous study [53]. It should be noted that these effective anti-icing service lives are conservatively calculated, because beyond them there are still residual friction benefits of this functional overlay, because part of the overlay surface would still be able to keep the moisture in a liquid instead of frozen state.

Sensitivity analysis

Sensitivity analysis was conducted to investigate how the C of the overlay was affected by variations in the overlay thickness (h) and D_{mastic} , because the simulation

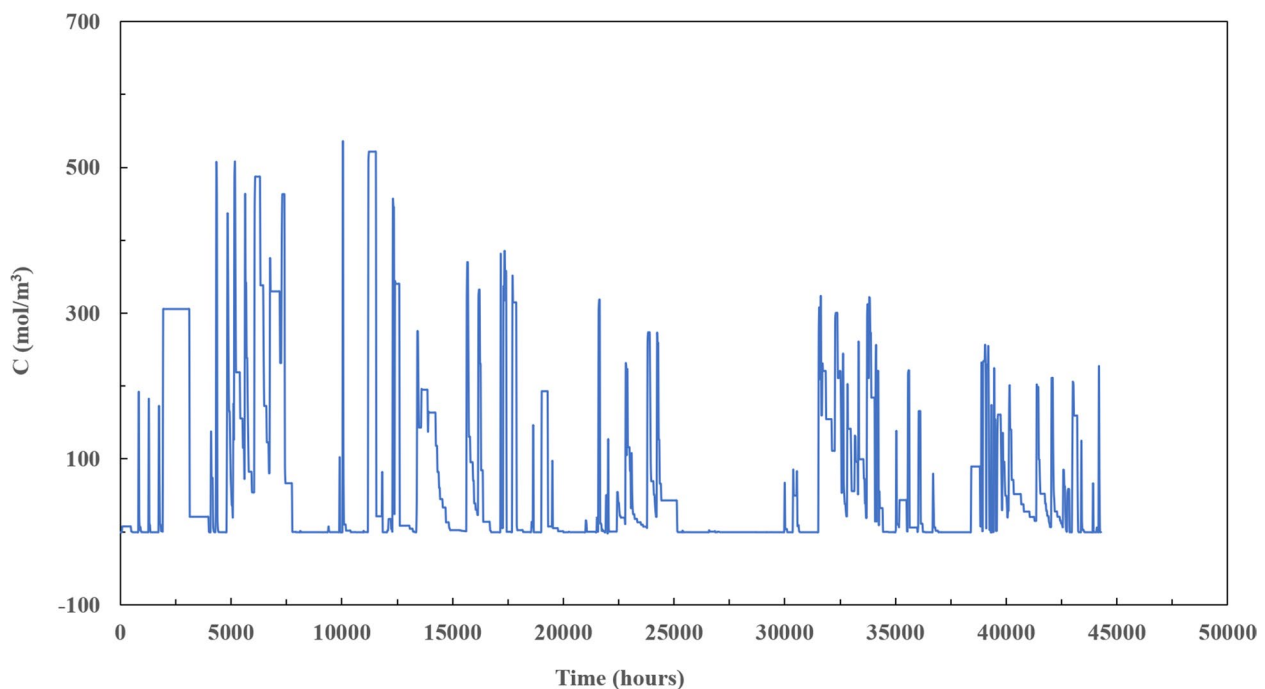
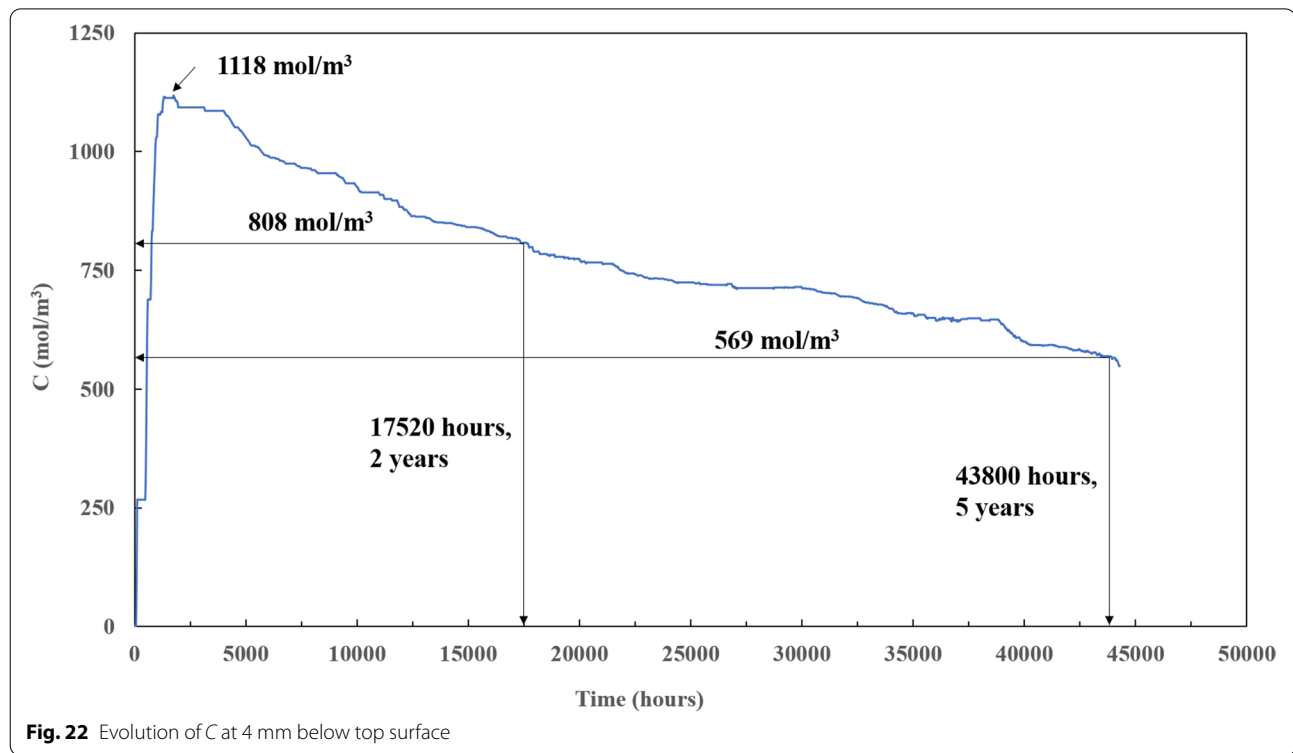


Fig. 21 Evolution of C on top surface



suggested that these two were dominant factors in determining the C of the overlay. With other parameters unchanged, the simulation model was re-run when the thickness of the geometry in Fig. 2c or D_{mastic} was increased or decreased by 20%.

The results of the water transport model under the new settings were very similar to or the same as those under the original setting, while the changes in h and D_{mastic} had more pronounced effects on the results of the chloride transport model. Under the new settings, the values of the C on top surface or in functional additives at a same point of time slightly changed from those under

the original setting. Figure 23a depicts the variation of the C over time at 4 mm below the top surface as a function of the h and D_{mastic} settings, over the simulated 43,800 h (5 years). In the first 1,500 h, as shown in Fig. 23b, the C decreased with reducing h or D_{mastic} , and a combined action of reducing both h and D_{mastic} further decreased the C . In contrast, the C increased with increasing h or D_{mastic} , and the C further increased when h and D_{mastic} increased simultaneously. For a long-term evaluation (as shown in Fig. 23a), interestingly, the reduction of D_{mastic} or both D_{mastic} and h resulted in slight increase in the C on the top surface of the overlay, likely due to a smaller amount of chloride ions being removed by precipitations. The other six changes of the parameters slightly decreased the C , indicative of multiple mechanisms at work.

Table 4 shows the predicted anti-icing life of the functional overlay for the different settings, assuming the goal is to prevent the surface from icing for 96.3% of the snow events. Under the original setting ($h=16$ mm, $D_{\text{mastic}}=\text{Eq. 27}$), the anti-icing function of the overlay is predicted to be effective for the overlay temperature above -2.4 °C, and the corresponding Cl^- concentration was 557 mol/m^3 , as shown in Table 3. Compared with the original setting, the anti-icing life of the overlay increased by 2% when D_{mastic} decreased by 20% and increased by 1% when both D_{mastic} and h decreased by 20%. On the other hand, it decreased by 6%, 9%, 9%, 10%, 1%, and 11% when D_{mastic} increased by 20%, h decreased by 20%, h increased

Table 3 Effective Cl^- concentration in water for anti-icing at specific temperatures

Temperature, °C	Cl Conc. in water for anti-icing, mol/ m^3
-1	228
-2	462
-2.4	557
-3	702
-3.4	800
-4	948
-4.6	1099
-5	1201

by 20%, both D_{mastic} and h increased by 20%, D_{mastic} decreased by 20% and h increased by 20%, and D_{mastic} increased by 20% and h decreased by 20% respectively.

Indirect validation of the predictive model

This study is limited to exploratory investigation. The finite element method-based model was built by following first principles of water and chloride transport, incorporated experimental results from laboratory, and

relying on case study data and assumptions where necessary. For the prediction of anti-icing life of the overlay with the functional additive, direct validation of this model remains challenging due the lack of directly usable data in the published domain and the lack of resources to conduct long-term laboratory or field investigation for longevity validation. Nonetheless, this section describes encouraging results that indirectly validate the predictive model established thus far.

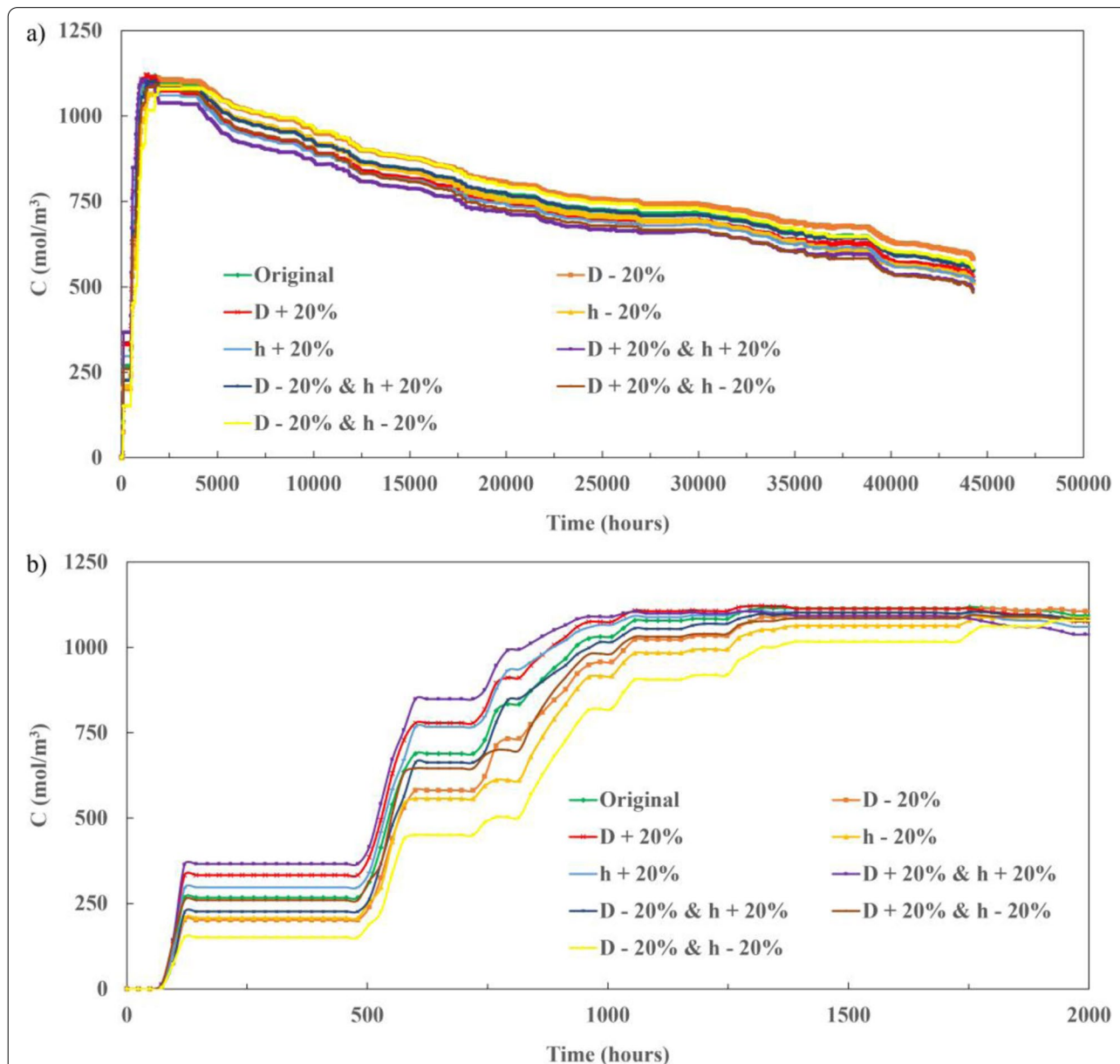


Fig. 23 Evolution of C at 4 mm below top surface based on different settings. **a** full-scale figure and **b** local enlarged figure. $D - 20\%$: reducing D_{mastic} by 20%; $D + 20\%$: increasing D_{mastic} by 20%; $h - 20\%$: reducing thickness by 20%; $h + 20\%$: increasing thickness by 20%; $D + 20\% \& h + 20\%$: increasing D_{mastic} by 20% and increasing thickness by 20%; $D - 20\% \& h + 20\%$: reducing D_{mastic} by 20% and increasing thickness by 20%; $D + 20\% \& h - 20\%$: increasing D_{mastic} by 20% and reducing thickness by 20%; $D - 20\% \& h - 20\%$: reducing D_{mastic} by 20% and reducing thickness by 20%

Figure 24 displays the temporal evolution of water fraction on the top surface vs. at center point of the overlay, and temporal evolution of chloride concentration at center point of the overlay vs. in an additive near center point, up to 1500 h. The variations of water fraction on the top surface of the overlay closely matches the pattern of how precipitation occurred on an hourly basis. It can be clearly seen that the water fraction at the center point rapidly increases during precipitations, whereas it gradually decreases due to natural water evaporations when there is no precipitation. Moreover, the chloride concentration at the center point increases over time when the water fraction is equal to or greater than 0.2, whereas the chloride concentration remains unchanged when the water fraction is less than 0.2. In contrast, the chloride concentration in the additive decreases over time when the water fraction is equal to or greater than 0.2, whereas it remains unchanged when the water fraction is less than 0.2. These predicted trends for both the water fraction and the chloride concentration at different points in the overlay are reasonable and consistent with the reality.

In our previous study [53], the results of the fog-freezing tests indicated the friction coefficient of the asphalt mixture with 5.1 wt% additive #16 decreased from 0.5 at -3.9°C to 0.4 at -9.4°C . This can be explained by the temporal evolution of the chloride concentration at a depth of 4 mm below the surface of the overlay. Figure 22 illustrates the predicted profile of the chloride concentration in the functional overlay at 1248 h. The model results indicate that the lowest temperature for an effective anti-icing of this overlay was about -4.6°C (corresponding to its highest chloride concentration of $1,118\text{ mol/m}^3$ on the plot, see Fig. 23a). At this temperature or above, all the water remained a liquid state and would not turn into ice. Thus, the anti-icing function was fully effective at -3.9°C , which explains the high friction coefficients from the fog-freezing

experiment at that temperature. It is apparent that $1,118\text{ mol/m}^3$ would not be sufficient to keep all the water (at the overlay surface) at a liquid state at -9.4°C ; instead, a minimum C of $2,400\text{ mol/m}^3$ is needed, by the theoretical evaluation based on the eutectic curve (see Figure S21). The simulation result at 1248 h revealed the chloride concentration at some locations at the 4-mm depth was higher than $2,400\text{ mol/m}^3$, as shown in the areas marked with purple ellipses in Fig. 25. These localized high chloride-concentration locations help explain the experimental result at -9.4°C . Because not all the water on the sample surface was prevented from icing, the friction coefficient reduced to 0.4 at -9.4°C from 0.5 at -3.9°C .

Conclusions

This study employed a Finite Element Method based software to predict the anti-icing life of a thin overlay of asphalt pavement with salt-storage additive, by simulating chloride transport in the overlay when exposed to the changes in weather conditions in terms of precipitation and temperature and pavement conditions in terms of thermal cracking and fatigue cracking. The FEM based simulation included water transport modeled with the “phtr” interface and chloride transport modeled with the “tds” interface of the software. The output of the water transport model was water fraction, which was used as one input parameter of the chloride transport model. The water fraction plays a crucial role in controlling the chloride diffusion coefficients of asphalt mastic and functional additive.

The results of the water transport model show the temporal and spatial evolutions of the water fraction in the overlay as a function of (historical) precipitation and pavement temperature. The water fraction increased rapidly during precipitations, whereas it gradually decreased due to water evaporation through the surface of the overlay when there was no precipitation. It was easier to lose water at the locations near the surface of the overlay than that around the middle and bottom. Pavement temperature was a variable affecting many parameters of the model, thus affecting the water fraction. These parameters included entry capillary pressure of water in pores of asphalt mastic and functional additive, dynamic viscosity of water and air, and density of air.

For the chloride transport model, the chloride concentration in asphalt mastic highly depended on the value of the water fraction, i.e., moisture availability limited the Cl^- diffusion coefficients of asphalt mastic and functional additive. The two Cl^- diffusion coefficients were equal to 0 when the water fraction was lower than 0.2. As the water fraction was equal to or higher than 0.2, the Cl^- diffusion coefficient of asphalt mastic was defined as a function of the surrounding chloride concentration,

Table 4 Predicted anti-icing life of overlay for different settings when percentile = 96.3%

Item	Anti-icing life, hour	Anti-icing life, year	Percentage change based on original
Original	43,800	5.00	0%
$D-20\%$	44,616	5.09	2%
$D+20\%$	41,256	4.71	-6%
$h-20\%$	39,840	4.55	-9%
$h+20\%$	39,816	4.55	-9%
$D+20\% \& h+20\%$	39,288	4.48	-10%
$D-20\% \& h+20\%$	43,200	4.93	-1%
$D+20\% \& h-20\%$	39,072	4.46	-11%
$D-20\% \& h-20\%$	44,064	5.03	1%

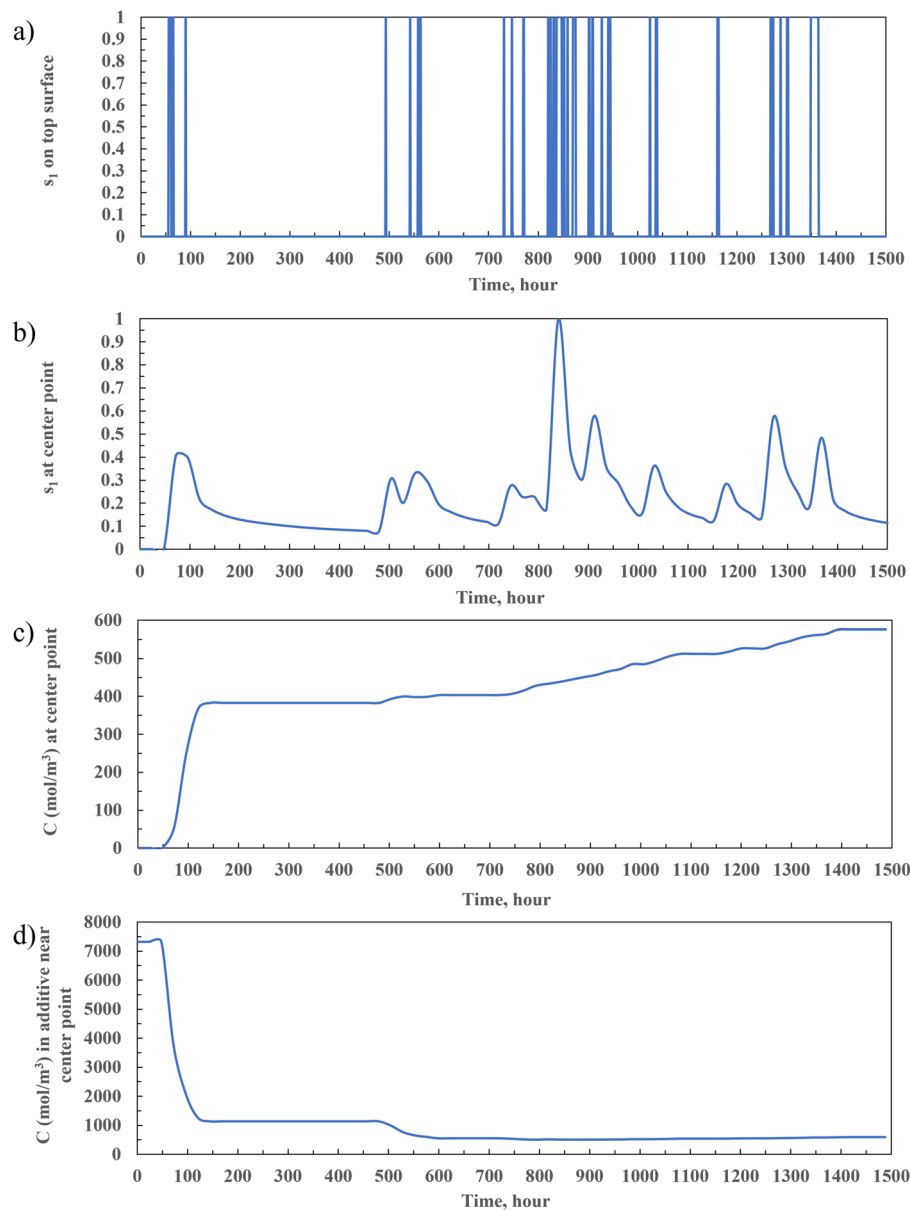


Fig. 24 Temporal evolution of water fraction (a) on the top surface vs. (b) at center point of the overlay, and temporal evolution of chloride concentration (c) at center point of the overlay vs. (d) in an additive near center point, up to 1500 h

pavement temperature, pavement thermal cracking, and pavement fatigue cracking, and the Cl^- diffusion coefficient of functional additive remained constant. Chloride ions migrated from high-concentration locations to low-concentration ones when the water fraction was equal to or higher than 0.2, until a balanced concentration profile was obtained in the system. The chloride concentration in asphalt mastic increased over time and the chloride concentration in functional additive decreased over time when the water fraction was equal to or higher than

0.2, otherwise it remained unchanged. Due to chloride removal on the top surface, the chloride concentration near the top surface was lower than that around the middle and bottom of the overlay.

Although the model considered the effect of pavement thermal cracking and fatigue cracking on increasing the Cl^- diffusion coefficient of asphalt mastic, other pavement distresses (moisture damage, rutting, longitudinal cracking, UV aging, etc.) and the interactions among these distresses were not included. Additional research is

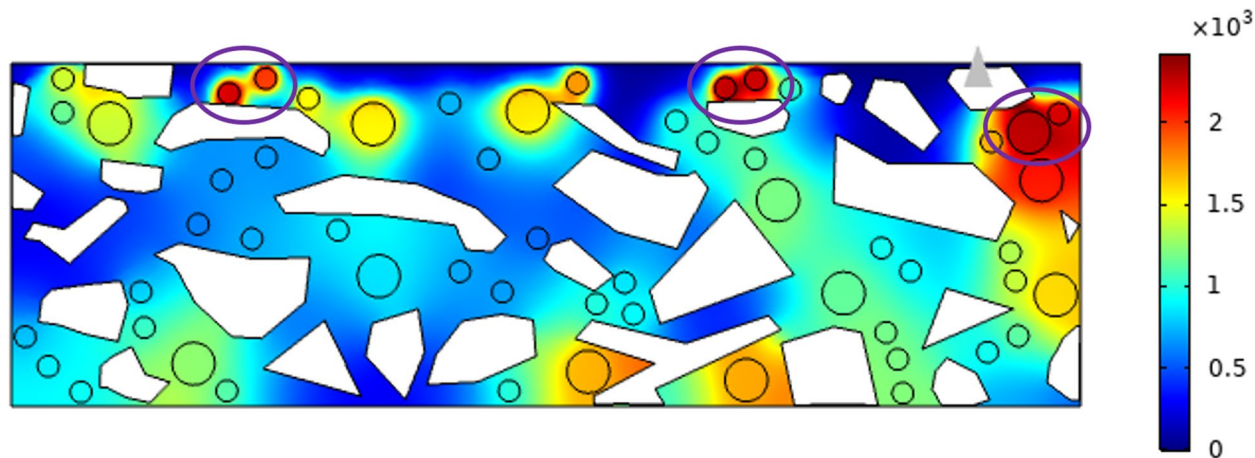


Fig. 25 Profile of C in the overlay at 1248 h

needed to further improve this model to allow better representation of the field behavior of the overlay over the long run, under various service environments.

This study revealed that the anti-icing function of the overlay was fully effective in 2 years and 5 years for the minimum pavement temperature above -3.4°C and -2.4°C , corresponding to its lowest chloride concentration of 808 mol/m^3 and 569 mol/m^3 at 4 mm depth of the 16-mm overlay, respectively. These two pavement temperatures translate to 97.4-percentile and 96.3-percentile of historical hourly pavement temperature near Pullman, WA, respectively. This was consistent with the estimated effective anti-icing life (5.0 years for the sample with 5.1 wt% additive #16) based on Eq. 3.2 in our previous study [53]. The current setting of the overlay thickness (16 mm) and the Cl^- diffusion coefficient of asphalt mastic (Eq. 27) also predicts a 96.3-percentile effective anti-icing life of 5.00 years, whereas the sensitivity analysis revealed that 20% changes in the overlay thickness or the Cl^- diffusion coefficient of asphalt mastic would change this service life to 4.55 to 5.09 years.

Abbreviations

APSSA: Asphalt pavement with salt-storage additive; phtr: Phase transport in porous media; tds: Transport of diluted species; SSA: Salt-storage additive; CaCl_2 -zeolite/p-epoxy: Laboratory-prepared functional additive; CaCl_2 : Calcium chloride; ϵ_p : Porosity of porous media; ρ_i : Density of phase i ; s_i : Volume fraction of phase i ; u_i : Volumetric flux (velocity vector) of phase i ; k_{pi} : Relative permeability of phase i ; μ_i : Dynamic viscosity of phase i ; g : Gravitational acceleration vector; p_c : Capillary pressure; p_{s_i} : Pressure in the non-wetting phase; p_{s_w} : Pressure in the wetting phase; s_w : Effective volume fraction of the wetting phase; s_w : Volume fraction of the wetting phase; s_{rw} : Residual volume fraction of the wetting phase; s_{rn} : Residual volume fraction of the non-wetting phase; k_{rs_w} : Relative permeability of the wetting phase; k_{rs_n} : Relative permeability of the non-wetting phase; \bar{s}_n : Effective volume fraction of the non-wetting phase; s_n : Volume fraction of the non-wetting phase; s_1 : Volume fraction of water; s_2 : Volume fraction of air; C : Chloride concentration; t : Time; D : Chloride diffusion coefficient; x : A position variable; C_i : Concentration of species i ; J_i : Diffusive flux vector; R_i : A reaction rate expression for species i ; D_i : Diffusion coefficient of

species i ; AutoCAD: Computer-aided design and drafting software; P_{ec} : Entry capillary pressure; σ : Interfacial tension of a fluid; θ : Contact angle between the fluid and the capillary tube; r_c : Radius of the capillary tube; K : Kelvin; SEM: Scanning electron microscope; r_c : Average value of the pore's radii; AV%: Air void percentage or porosity in asphalt mastic; D_{75} : Particle-size diameter corresponding to 75% on the cumulative particle-size distribution curve of aggregates; $\lambda_{p-epoxy}$: Pore size distribution index; W_i : Weight fraction of pores; N_i : Number of pores; A_i : Surface area of pores; $\lambda_{p-mastic}$: Pore size distribution index of asphalt mastic; k_{mastic} : Water permeability of asphalt mastic; ρ : Density; μ : Dynamic viscosity; s_r : Residual saturation; $s_{0,1}$: Initial value of the water volume fractions; $C(x,t)$: Chloride concentration at a location x at a time t ; C_s : Chloride concentration at surface; C_0 : Initial chloride concentration at location x ; $\text{erf}(z)$: Error function; D_{ss} : Steady-state chloride diffusion coefficient; A_c : C-related coefficient to D ; D_0 : Maximal chloride diffusion coefficient; E_a : Activation energy for diffusion; R : Universal gas constant; T : Absolute temperature of asphalt pavement; A_T : T-related coefficient to D ; T_i : Testing temperature of the mastic diffusion test; T_a : Air temperature; R_s : Daily solar radiation; d : Depth from pavement surface; C_{ave} : Average chloride concentration; N_n : Number of the non-cracking 150 mm sections; C_n : Chloride concentration at the bottom of the geometry of a non-cracking 150 mm section; N_c : Number of the 1-crack 150 mm sections; C_c : Chloride concentration at the bottom of the geometry of a 1-crack 150 mm section; A_{tc} : Thermal cracking-related coefficient to D ; ESALs: Equivalent single axle loads; LEF: Load equivalency factor; LTPP: Long-term pavement performance; L : Length of the transverse fatigue crack; A_{fc} : Fatigue cracking-related coefficient to D ; D_{mastic} : Chloride diffusion coefficient of asphalt mastic; $D_{additive}$: Chloride diffusion coefficient in the additives; $C_{initial}$: Initial value of the chloride concentration in the additives; $\text{Ca}(\text{NO}_3)_2 \cdot 6\text{H}_2\text{O}$: Calcium nitrate tetrahydrate; H_1 : Initial height of water in standpipe; H_2 : Final height of water in standpipe; A_1 : Cross-sectional area of sample; A_2 : Cross-sectional area of standpipe; L_s : Length of sample; μ_w : Dynamic viscosity of water at 25°C ; ρ_w : Density of water; C_{CaCl_2} : Effective mass percentage of CaCl_2 for anti-icing at a temperature; h : Overlay thickness; FEM: Finite element method.

Supplementary Information

The online version contains supplementary material available at <https://doi.org/10.1186/s43065-021-00047-w>.

Additional file 1: Figure S1. Relationship between σ of water and pavement temperatures. **Figure S2.** Particle-size distribution curve of aggregates used for asphalt mixture. **Figure S3.** Relationship between μ of water and pavement temperatures. **Figure S4.** Relationship between μ of air and pavement temperatures. **Figure S5.** Relationship between ρ of air and pavement temperatures. **Figure S6.** a) Simulated and calculated C-time curves and b) goodness of fit at 0% cracking level for thermal cracking. **Figure S7.** a) Simulated and calculated C-time curves and b) goodness of fit at 27% cracking

level for thermal cracking. **Figure S8.** a) Simulated and calculated C-time curves and b) goodness of fit at 38% cracking level for thermal cracking. **Figure S9.** a) Simulated and calculated C-time curves and b) goodness of fit at 59% cracking level for thermal cracking. **Figure S10.** ESALS-fatigue crack rate relationship of asphalt pavement. **Figure S11.** ESALS-crack width relationship of asphalt pavement. **Figure S12.** Loading number-crack width relationship of asphalt pavement. **Figure S13.** Load-single LEF relationship of asphalt pavement. **Figure S14.** Crack width-crack depth relationship of asphalt pavement. **Figure S15.** a) Simulated and calculated C-time curves and b) goodness of fit at 0 year for fatigue cracking. **Figure S16.** a) Simulated and calculated C-time curves and b) goodness of fit at 8 years for fatigue cracking. **Figure S17.** a) Simulated and calculated C-time curves and b) goodness of fit at 9 years for fatigue cracking. **Figure S18.** a) Simulated and calculated C-time curves and b) goodness of fit at 10 years for fatigue cracking. **Figure S19.** a) C-time curves from simulation and experiment and b) goodness of fit to determine D of additives (datapoints before 71 h were removed in Figure S19b due to unstable diffusion). **Figure S20.** a) Cl concentration-time relationship and b) Cl diffusion coefficient-time relationship from mastic diffusion test. **Figure S21.** Phase diagram for water-CaCl₂ system (adopted from Phase diagrams for binary salt solutions | Phasediagram). **Table S1.** a) Area fractions of asphalt mastic, aggregates, and additives in each of samples. **Table S2.** An example of calculating $\lambda_{p-epoxy}$ for Figure 2. **Table S3.** Estimated $\lambda_{p-epoxy}$ based on three SEM images of the surface of CaCl₂-zeolite/p-epoxy #16. **Table S4.** Time-ESALS datapoints. **Table S5.** # of 150-mm sections over time related to fatigue cracking of asphalt pavement. **Table S6.** Total depth, width, and partial depth (in the model) of the transverse fatigue crack at different years. **Table S7.** Parameters and results of falling head test. **Table S8.** Results of water contact angle test.

Acknowledgements

The authors also would like to acknowledge professional engineers Alex Guo and Yue Huang who work for COMSOL Inc. for their tremendous help in using the software.

Authors' contributions

Y. Zhang did final interpretation of the results of all the tests, established part of the model with COMSOL Multiphysics, and wrote part of the draft manuscript. Y. Deng established part of the model with COMSOL Multiphysics and wrote part of the draft manuscript. X. Shi designed the scope of this work and advised the team throughout the process (from conceptualization to manuscript preparation). All authors read and approved the final manuscript.

Funding

The authors thankfully acknowledge financial support by the Tier 1 University Transportation Center CESTICC (Center for Environmentally Sustainable Transportation in Cold Climates).

Availability of data and materials

The datasets generated and/or analyzed during the current study are available upon request.

Declarations

Competing interests

The authors declare no competing interest.

Received: 13 October 2021 Accepted: 29 November 2021

Published online: 04 January 2022

References

- ASTM D5084 2020 Test Methods for Measurement of Hydraulic Conductivity of Saturated Porous Materials Using a Flexible Wall Permeameter ASTM International <https://doi.org/10.1520/D5084-03>
- Bentz DP, Garboczi EJ, Lu Y, Martys N, Sakulich AR, Weiss WJ (2013) Modeling of the influence of transverse cracking on chloride penetration into concrete. *Cem Concr Compos* 38:65–74. <https://doi.org/10.1016/j.cemconcomp.2013.03.003>
- Bogdanov, I.I., El Ganaoui, K., Kamp, A.M., 2007. COMSOL 2D Simulation of Heavy Oil Recovery by Steam Assisted Gravity Drainage. *Proc. Eur. COMSOL Conf.*
- Brooks B, R.H., Corey, A.T., (1964) Hydraulic properties of porous media. *Diss Colo. State Univ, Libr*
- Brooks RH, Corey AT (1966) Properties of Porous Media Affecting Fluid Flow. *J Irrig Drain Div* 92:61–88
- de Vera G, Climent MA, Viqueira E, Antón C, Andrade C (2007) A test method for measuring chloride diffusion coefficients through partially saturated concrete. Part II: The instantaneous plane source diffusion case with chloride binding consideration. *Cem Concr Res* 37:714–724
- Dickinson EJ, Ekström H, Fontes E (2014) COMSOL Multiphysics®: Finite element software for electrochemical analysis. A mini-review *Electrochem Commun* 40:71–74
- Djerbi A, Bonnet S, Khelidj A, Baroghel-bouny V (2008) Influence of traversing crack on chloride diffusion into concrete. *Cem Concr Res* 38:877–883
- Garboczi EJ, Bentz DP, Davis JM, Lu Y (2012) Modeling Chloride transport in Cracked Concrete: A 3-D image-based microstructure simulation 1–15
- Gittens GJ (1969) Variation of surface tension of water with temperature. *J Colloid Interface Sci* 30:406–412
- Giuliani F, Merusi F, Polacco G, Filippi S, Paci M (2012) Effectiveness of sodium chloride-based anti-icing filler in asphalt mixtures. *Constr Build Mater* 30:174–179
- Gu C, Ye G, Sun W (2015) A review of the chloride transport properties of cracked concrete: experiments and simulations. *J Zhejiang Univ-Sci. A* 16:81–92
- Hall JR, Wishaw BF, Stokes RH (1953) The diffusion coefficients of calcium chloride and ammonium chloride in concentrated aqueous solutions at 25. *J Am Chem Soc* 75:1556–1560
- Hoplin C (2016) Cracking Performance Evaluation of Minnesota Asphalt Pavements
- Islam, M., 2015. THERMAL FATIGUE DAMAGE OF ASPHALT PAVEMENT. *Civ. Eng. ETDs*.
- Joekar-Niasar V, Hassanizadeh SM, Leijnse A (2008) Insights into the Relationships Among Capillary Pressure, Saturation, Interfacial Area and Relative Permeability Using Pore-Network Modeling. *Transp Porous Media* 74:201–219
- Kanarakaj U, Lhaden T, Karthik Raj V (2015) Analysis of structural mechanics of solid microneedle using COMSOL software, in: 2015 International Conference on Innovations in Information, Embedded and Communication Systems (ICIIECS). pp 1–5 (Presented at the 2015 International Conference on Innovations in Information, Embedded and Communication Systems (ICIIECS))
- Khan MU, Ahmad S, Al-Gahtani HJ (2017) Chloride-Induced Corrosion of Steel in Concrete: An Overview on Chloride Diffusion and Prediction of Corrosion Initiation Time. *Int. J. Corros* 2017:e5819202
- Kwon SJ, Na UJ, Park SS, Jung SH (2009) Service life prediction of concrete wharves with early-aged crack: Probabilistic approach for chloride diffusion. *Struct Saf* 31:75–83. <https://doi.org/10.1016/j.jstrsafe.2008.03.004>
- Li Q, Ito K, Wu Z, Lowry CS, Li SPL (2009) COMSOL Multiphysics: A Novel Approach to Ground Water Modeling. *Groundwater* 47:480–487
- Li Y (1999) Asphalt Pavement Fatigue Cracking Modeling
- Liu Y, Shi X (2012) Ionic transport in cementitious materials under an externally applied electric field: Finite element modeling. *Constr Build Mater* 27:450–460
- Liu Y, Shi X (2012) Stochastic Modeling of Service Life of Concrete Structures in Chloride-Laden Environments. *J Mater Civ Eng* 24:381–390
- Liu Z, Xing M, Chen S, He R, Cong P (2014) Influence of the chloride-based anti-freeze filler on the properties of asphalt mixtures. *Constr Build Mater* 51:133–140
- Ma T, Geng L, Ding X, Zhang D, Huang X (2016) Experimental study of deicing asphalt mixture with anti-icing additives. *Constr Build Mater* 127:653–662
- Ma, X., Cheng, B., Mao, J., Liu, W., Zi, D., 2009. Finite element modeling of coupled heat and moisture transfer in typical earth-sheltered building envelope. *Proc. Elev. Int. IBPSA Conf. Glasg. Scotl. Build. Simul.* 1850–1856.
- Montgomery RB (1947) VISCOSITY AND THERMAL CONDUCTIVITY OF AIR AND DIFFUSIVITY OF WATER VAPOR IN AIR. *J Atmospheric Sci* 4:193–196

28. Nardi A, Idiart A, Trinchero P, de Vries LM, Molinero J (2014) Interface COMSOL-PHREEQC (iCP), an efficient numerical framework for the solution of coupled multiphysics and geochemistry. *Comput Geosci* 69:10–21
29. Nielsen EP, Geiker MR (2003) Chloride diffusion in partially saturated cementitious material. *Cem Concr Res* 33:133–138
30. Page CL, Short NR, El Tarras A (1981) Diffusion of chloride ions in hardened cement pastes. *Cem Concr Res* 11:395–406
31. Paul SK, Chaudhuri S, Barai SV (2014) Chloride diffusion study in different types of concrete using finite element method (FEM). *Adv Concr Constr* 2:39–56
32. Rachedi BA, Babouri A, Berrouk F (2014) A study of electromagnetic field generated by high voltage lines using COMSOL MULTIPHYSICS. 2014 International Conference on Electrical Sciences and Technologies in Maghreb (CISTEM). pp 1–5 (Presented at the 2014 International Conference on Electrical Sciences and Technologies in Maghreb (CISTEM))
33. Saadoun T, Garcia A, Gómez-Mejide B (2017) Dynamics of water evaporation in cold asphalt mixtures. *Mater Des* 134:196–206
34. Solaimanian, M., Thomas, W.K., 1993. Predicting maximum pavement surface temperature using maximum air temperature and hourly solar radiation. *Transp. Res. Rec.* 1–1.
35. Spragg RP, Castro J, Li W, Pour-Ghaz M, Huang P-T, Weiss J (2011) Wetting and drying of concrete using aqueous solutions containing deicing salts. *Cem Concr Compos* 33:535–542
36. Tan, Y., Wang, S., Xu, F., Liu, W., Chen, X., Liang, Y., 2017. Application of COMSOL Multiphysics in Research of Concrete Durability-A Short Review. *J. Chin. Ceram. Soc.* 05.
37. Tang L (1999) Concentration dependence of diffusion and migration of chloride ions: Part 2. Experimental evaluations *Cem Concr Res* 29:1469–1474
38. Taylor DW (1956) *Fundamentals of Soil Mechanics* 100
39. Transportation Officials, 1993. *AASHTO Guide for Design of Pavement Structures*. Aashto Vol. 1.
40. Truc O, Ollivier JP, Carcassès M (2000) A new way for determining the chloride diffusion coefficient in concrete from steady state migration test. *Cem Concr Res* 30:217–226
41. Vardanega PJ, Waters TJ (2011) Analysis of Asphalt Concrete Permeability Data Using Representative Pore Size. *J Mater Civ Eng* 23:169–176
42. Vennard JK, Street RL (1975) *Elementary Fluid Mechanics*, 5th edn. Wiley, NY
43. Wang, C.Y., 1998. Modeling multiphase flow and transport in porous media. *Transp. Phenom. Porous Media* 383–410.
44. Wang CY, Cheng P (1996) A multiphase mixture model for multiphase, multicomponent transport in capillary porous media—I. Model development. *Int J Heat Mass Transf* 39:3607–3618
45. Wang X-Y, Zhang L-N (2016) Simulation of Chloride Diffusion in Cracked Concrete with Different Crack Patterns. *Adv. Mater. Sci. Eng* 2016:e1075452
46. Wegner, J., Ganzer, L., 2012. Numerical Simulation of Oil Recovery by Polymer Injection using COMSOL. *Excerpt Proc. 2012 COMSOL Conf. Milan*.
47. Wei Z, Weavers LK (2016) Combining COMSOL modeling with acoustic pressure maps to design sono-reactors. *Ultrason Sonochem* 31:490–498
48. Wu LZ, Zhang LM, Zhou Y, Li BE (2017) Analysis of multi-phase coupled seepage and stability in anisotropic slopes under rainfall condition. *Environ Earth Sci* 76:469
49. Yang P, Dhandapani Y, Santhanam M, Neithalath N (2020) Simulation of chloride diffusion in fly ash and limestone-calcined clay cement (LC3) concretes and the influence of damage on service-life. *Cem. Concr. Res* 130:106010
50. Yuan, Q., Shi, C., De Schutter, G., Audenaert, K., 2008. Effect of temperature on transport of chloride ions in concrete. *Concr. Repair Rehabil. Retrofit*. II CRC Press. 159–160.
51. Zamel N, Li X (2008) A parametric study of multi-phase and multi-species transport in the cathode of PEM fuel cells. *Int J Energy Res* 32:698–721
52. Zhang P, Li D, Qiao Y, Zhang S, Sun C, Zhao T (2018) Effect of Air Entrainment on the Mechanical Properties, Chloride Migration, and Microstructure of Ordinary Concrete and Fly Ash Concrete. *J Mater Civ Eng* 30:04018265
53. Zhang Y, Shi X (2021) Laboratory evaluation of a sustainable additive for anti-icing asphalt. *Cold Reg. Sci. Technol* 189:103338
54. Zhao XH, Zhang XD (2011) The Research on the Anti-Icing and Pavement Performance of the Chloride-Store Asphalt Mixture. *Appl Mech Mater* 97–98:321–326
55. Zheng M, Wang C, Han L, Sun Y, Li Y, Ma Z (2016) Laboratory evaluation of long-term anti-icing performance and moisture susceptibility of chloride-based asphalt mixture. *Int J Pavement Res Technol* 9:140–148
56. Zheng M, Zhou J, Wu S, Yuan H, Meng J (2015) Evaluation of long-term performance of anti-icing asphalt pavement. *Constr Build Mater* 84:277–283
57. Zhong K, Sun M, Chang R (2018) Performance evaluation of high-elastic/salt-storage asphalt mixture modified with Mafilon and rubber particles. *Constr Build Mater* 193:153–161
58. Zhou J, Li J, Liu G, Yang T, Zhao Y (2019) Long-Term Performance and Deicing Effect of Sustained-Release Snow Melting Asphalt Mixture. *Adv Civ Eng* 2019:1940692. <https://doi.org/10.1155/2019/1940692>

Publisher's Note

Springer Nature remains neutral with regard to jurisdictional claims in published maps and institutional affiliations.

Submit your manuscript to a SpringerOpen[®] journal and benefit from:

- Convenient online submission
- Rigorous peer review
- Open access: articles freely available online
- High visibility within the field
- Retaining the copyright to your article

Submit your next manuscript at ► [springeropen.com](https://www.springeropen.com)